Role of atmospheric horizontal resolution in simulating tropical and subtropical South American precipitation in HadGEM3-GC31

Paul-Arthur Monerie[1], Amulya Chevuturi[1], Peter Cook[1], Nick Klingaman[1], Christopher E. Holloway[2]

[1] Department of Meteorology, National Centre for Atmospheric Science (NCAS), University of Reading, Reading, UK

[2]Department of Meteorology, University of Reading, Reading, UK

Correspondence to: Paul-Arthur Monerie (pmonerie@gmail.com)

Abstract

We assess the effect of increasing horizontal resolution on simulated precipitation over South America in a climate model. We use atmosphere-only simulations, performed with HadGEM3-GC31 at three horizontal resolutions: N96 (~130 km, 1.88° x 1.25°), N216 (~60 km, 0.83° × 0.56°), and N512 (~25 km, 0.35° x 0.23°). We show that all simulations have systematic biases in annual mean and seasonal mean precipitation over South America (e.g. too wet over the Amazon and too dry in northeast). Increasing horizontal resolution improves simulated precipitation over the Andes and northeast Brazil. Over the Andes, improvements from horizontal resolution continue to ~25km, while over northeast Brazil, there are no improvements beyond ~60km resolution. These changes are primarily related to changes in atmospheric dynamics and moisture flux convergence. Over the Amazon basin, precipitation variability increases at higher resolution. We show that some spatial and temporal features of daily South American precipitation are improved at high resolution, including the intensity spectra of rainfall. Spatial scales of daily

precipitation features are also better simulated, suggesting that higher resolution may improve the representation of South American mesoscale convective systems.

1. Introduction

South America is a large area encompassing tropical, sub-tropical and extratropical climates. The Andes covers western South America, from South to North, while the eastern part of South America is flatter than the west. The Amazon basin has high mean rainfall and is covered by a rainforest, while northeastern Brazil is semi-arid. Several climatic areas are thus often defined to account for the climatic heterogeneity of South America, with focus specifically on the Andes, the Amazon Basin, northeast Brazil and southeast Brazil (Custodio et al., 2017).

Climate models have biases in simulating South American precipitation, partly due to biases in simulating teleconnections between both Atlantic and Pacific sea-surface temperatures (SSTs), and precipitation over land (Bombardi and Carvalho, 2008; Coelho et al., 2016; Jung et al., 2011; Koutroulis et al., 2016; Sierra et al., 2015; Yin et al., 2013). At sub-seasonal scales, precipitation variability is associated with the Madden—Julian Oscillation (MJO) (Grimm, 2019). The MJO modulates precipitation over South America, leading to either anomalously dry or wet conditions, depending on its phase. The MJO also favors extreme events, leading to droughts and floods (Grimm, 2019). At inter-annual scales, the El Niño Southern Oscillation (ENSO) strongly impacts Amazon precipitation, with El Niño events related to droughts (Grimm and Silva Dias, 1995; Grimm and Tedeschi, 2009; Lewis et al., 2011; Marengo et al., 2008, 2011, 2013; Zeng et al., 2008). Variability in the tropical Atlantic Ocean modulates trade easterlies and impacts precipitation over northeast Brazil (Liu and Juárez, 2001; Zeng et al., 2008) and southeast Brazil (Coelho et al., 2016). On decadal to multi-decadal scales, variability in northeast Brazilian precipitation is tied to the Atlantic Multidecadal Variability, which is associated with the location of the Atlantic Intertropical Convergence Zone (ITCZ) (Knight et al., 2006). Brazilian precipitation is also associated with Interdecadal

Pacific Variability (IPV; Power et al. 1999), positive IPV phases reduce precipitation over South America (Villamayor et al., 2018). Errors in simulating teleconnections from local and remote SST variability leads to biases in the intensity, position of the ITCZ and the South Atlantic Convergence Zone (SACZ), which degrade simulated South American precipitation and temperature (Bombardi and Carvalho, 2008; Custodio et al., 2017; Custódio et al., 2012).

Besides teleconnections, climate variability results from complex local interactions between energy, precipitation and soil moisture. These feedbacks are particularly strong over interior South America, one of the "hot spots" in soil moisture—precipitation coupling (Koster et al., 2004; Wei and Dirmeyer, 2012). Variability in recycling accounts for a large fraction of precipitation variability over northeastern Brazil and the La Plata Basin (Sörensson and Menéndez, 2011). Soil moisture memory influences atmospheric variability and could affect the development of the South American Monsoon System (Vera et al., 2006). Therefore, biases in simulated South American climate may be partly attributed to biases in local land-atmosphere coupling.

Improving simulated precipitation in climate models may also improve subseasonal-to-decadal predictions, because the performance of initialised forecasts and free-running models relies on the representation of key physical processes, such as convection and land-atmosphere feedbacks. For instance, models with the largest systematic errors produce the lowest precipitation prediction performance (DelSole and Shukla, 2010). Jia et al. (2014) showed that the high-resolution version of the GFDL model produces lower biases and higher skill for seasonal variations of 2-m air temperature and precipitation over South America, than its lower-resolution counterpart. Therefore, Doblas-Reyes et al. (2013) proposed that increasing spatial resolution is one of the main challenges for improving predictions.

Horizontal resolutions of Coupled Model Intercomparison Project (CMIP; Taylor et al. 2012; Eyring et al. 2016) models are typically ~150 km, or coarser, in the atmosphere, and ~100 km in the ocean. Important climate processes, such as atmospheric convection, and mesoscale boundary currents and eddies, have to

71 be parameterized rather than resolved, which may compromise dynamical processes and dynamics-physics
72 interactions (Collins et al. 2018). A growing body of evidence shows then that increasing horizontal
73 resolution can improve some aspects of the simulated climate (Roberts et al. 2018, 2019; among others).
74 Higher-resolution ocean-atmosphere coupled models outperform lower-resolution models at simulating
75 SST over coastal upwelling regions, due to a better simulation of near-surface wind and its effect on the
76 ocean (Delworth et al., 2011; Gent et al., 2010; McClean et al., 2011; Sakamoto et al., 2012; Shaffrey et
77 al., 2009; Small et al., 2014). Resolution reduces the double ITCZ bias (Delworth et al., 2011) and improves
78 variability in the El-Niño Southern Oscillation (Sakamoto et al., 2012; Shaffrey et al., 2009; Small et al.,
79 2014) and north Atlantic SSTs (Gent et al., 2010). Jung et al. (2011) and Jia et al. (2014) highlighted that
80 increased resolution improved simulated South American precipitation and tropical mean precipitation, and
81 atmospheric circulation. Improved land precipitation is partly due to a better representation of orography
82 (Delworth et al., 2011; Gent et al., 2010; Sakamoto et al., 2012). Over South America, increasing horizontal
83 resolution improves the representation of climate patterns (Custodio et al., 2017), particularly over the
84 Ocean, over the Atlantic ITCZ and SACZ. Although strongly model and season dependent, high resolution
85 regional climate models also improve simulated precipitation and temperature over South America (Falco
86 et al., 2019; Solman and Blázquez, 2019). Increased resolution also affects local features, such as the
87 propagation of mesoscale systems (Vellinga et al., 2016) and local land-atmosphere feedbacks (Mueller et
88 al. under review).

89 However, horizontal resolution does not always improve simulated climate. Bacmeister et al. (2013) found
90 that the high-resolution Community Atmosphere Model (CAM) did not improve simulated South American
91 rainfall, compared to a lower-resolution configuration. Some simulations exhibit too much warming and
92 cooling, especially over polar regions where sea ice is not accurately represented (Kirtman et al., 2012;
93 McClean et al., 2011). Impacts of increased horizontal resolution strongly depend on the range of
94 resolutions considered, on the region, phenomena and spatial and temporal scales of interest (Jung et al.,

2011; Roberts et al., 2018). Therefore, there is a need to better understand how increasing the horizontal resolution could benefit simulated South American precipitation.

Accurate predictions and projections of extreme rainfall require realistic simulated precipitation distributions. However, models exhibit biases in the frequency and persistence of light (<10 $mm.day^{-1}$) and heavy precipitation (>20 $mm.day^{-1}$) (Dai, 2006; Koutroulis et al., 2016; Sun et al., 2006). Errors in precipitation frequency and intensity are related to biases in the global hydrological cycle, including evaporation recycling over land (Demory et al., 2014; Trenberth, 2011). Improved representations of intense small-scale events improves modelled precipitation variability in models over parts of South America (De Sales and Xue, 2011). These biases may be partly due to the coarse resolution of CMIP climate models; increased resolution could improve simulated extreme convective rainfall by enhancing smaller-scale precipitation features, as shown by Solman and Blázquez (2019) over South America.

High resolution models are costly; if higher resolution produces little or no improvements in model biases, then computational resources could be used elsewhere, such as in increased ensemble size or adding initialization dates in forecasting systems, or improved or additional model physics. The European Union's Horizon 2020 PRIMAVERA project (www.primavera-h2020.eu) uses the CMIP6 High Resolution Model Intercomparison Project (HighResMIP; Haarsma et al. 2016) protocol and aims to develop a new generation of advanced high-resolution global climate models.

We use PRIMAVERA simulations to evaluate whether increased horizontal resolution improves simulated South American precipitation. We address three main questions:

- What are the model biases in simulated precipitation over South America?

- Is South American mean precipitation and variability better simulated at higher than at lower resolution? What is the minimum resolution required to improve the lower resolution biases?

- Are the spatial and temporal organizations of precipitation, better simulated at higher resolution?

The paper is structured as follows: the model, data and methodology are described in Sect. 2. Sect. 3 focuses on the model's ability to simulate annual and seasonal precipitation mean. We discuss seasonal to interannual variability in Sect. 4 and daily to sub-seasonal variability and spatial and temporal scales of precipitation in Sect. 5. A conclusion is given in Sect. 6.

2. Data and Methods

2.1 HadGEM3-GC3.1

HadGEM3-GC3.1 (hereafter HadGEM3) (Williams et al., 2018) has been run in an atmosphere-only configuration for 1950-2014, forced by HadISST2 daily 0.25° SSTs and sea ice (Rayner et al., 2006). The atmospheric model is the Global Atmosphere 7.1 scientific configuration (Walters et al., 2019), with 85 vertical levels. A common historical forcing is imposed in all simulations, including SSTs, greenhouse gases and aerosols. Three sets of simulations are performed, which only differ by their horizontal resolution and by a stochastic perturbation of their initial conditions: N96 horizontal resolution (~130 km, 1.88° x 1.25°; HadGEM3-GC3.1-LM), N216 horizontal resolution (~60 km, 0.83° × 0.56°; HadGEM3-GC3.1-MM) and N512 horizontal resolution (~25 km, 0.35° x 0.23°; HadGEM3-GC3.1-HM). Three members were performed at each resolution, for a total of 9 simulations. The simulations are part of the European Union's Horizon 2020 PRIMAVERA project (www.primavera-h2020.eu) uses the CMIP6 High Resolution Model Intercomparison Project (HighResMIP; Haarsma et al. 2016).

2.2 Observations and reanalysis

To verify the spatial and temporal scales of rainfall, three-hour and daily mean precipitation from HadGEM3 is compared against a high-resolution (0.25° x 0.25°) satellite-derived product for 1998-2017: NOAA CPC Morphing Technique (CMORPH version 1; Joyce et al. 2004). To evaluate time-mean rainfall and sub-seasonal to seasonal variability, we compare HadGEM3 to longer-period, but lower-resolution, gauge-based datasets from the University of Delaware (Willmott et al., 2001) and from the Global Precipitation Climatology Centre (GPCC; Schneider et al. 2014), both at a 0.5° horizontal resolution. We assess mean circulation against the NCEP-NCAR reanalysis (Kanamitsu et al., 2002), given on a 2.5°

resolution (144 × 72) with 17 vertical levels, and ERA-interim reanalysis (Dee et al., 2011), given on a 1.5° horizontal resolution.

To assess biases and impacts of the horizontal resolution on mean annual and seasonal precipitation we used monthly data, over 1950-2014, using GPCC and NCEP reanalysis. For daily variance we used GPCC, over 1982-2014. For the analysis of the spatial scales in precipitation, we used CMORPH, over 1998-2014. Note that results in mean and variance in precipitation were also assessed with CMORPH, in addition to GPCC, for a consistency with the spatial scales analysis.

2.3 Data interpolation

Differences between HadGEM3 and observations and between HadGEM3 at different horizontal resolutions are assessed by first interpolating all data to a common 0.5° x 0.5° resolution. Results were repeated, with data interpolated onto a common coarser resolution, 2.5° x 2.5° grid, showing similar results. For the analysis of the spatial scales in precipitation, both simulations and observations are interpolated onto a common lower resolution, N96.

2.4 Analysis of Scales of Precipitation (ASoP)

The Analysis of Scales of Precipitation (ASoP; Klingaman et al. 2017; Martin et al. 2017) diagnostics provide information on the intensity spectra of precipitation, the contribution to total precipitation from precipitation events of various intensities, the temporal persistence of precipitation and the typical spatial and temporal scales of precipitation.

The intensity spectra measures intensity distributions by computing the contributions of discrete intensity bins to the total precipitation for each grid point, to be visualised as maps (at grid scale) or aggregated over regions into histograms. Spatial scales of precipitation features are measured by dividing the analysis domain into non-overlapping subregions and computing correlations of each point in the sub-region against

the central grid point, then averaging the resulting correlation maps over all sub-regions. Temporal scales are measured by auto-correlations at a range of lags. Further information can be found in Klingaman et al. (2017) and Martin et al. (2017).

Further, we measure the distribution of the duration of precipitation events in discrete intensity bins by constructing a two-dimensional (2-D) histogram of binned precipitation intensity against binned duration in that intensity bin. We calculate the 2-D histogram by aggregating data across the analysis domain, then normalised by the number of spatial and temporal points in the dataset, to compare across datasets. The ASoP and duration diagnostics are applied over two subregions of South America: Amazon (AMZ; 10°S – 5°N; 72°W – 50°W) and southeast South America (SESA; 35°S – 18°S; 63°W – 40°W). We apply these diagnostics to daily data on the native HadGEM3 and CMORPH grids, as well as a common N96 grid.

We produce a 1-D histogram for duration of dry spells, where a dry spell is defined as a time interval of consecutive precipitation events of less than 0.1 $mm.day^{-1}$. This histogram is normalized by number of spatial and temporal points in the dataset, to compare across datasets.

2.5 Coupling strength metric

Interactions between soil moisture, precipitation, temperature and evaporation modulate climate variability. We assess the sensitivity of coupling strength between these variables to resolution. Coupling strength is defined, at each grid point, after removing the linear trend and seasonal cycle, and on the daily time scale, as

$$r_{a,b}\sigma_b = cor(a,b) \times std(b)$$

Where *cor(a, b)* is the correlation between the variables *a* and *b* and *std* is the standard deviation. As an example, for the coupling strength between soil moisture (in the top 0.1m of soil) and latent heat flux, *a* is the soil moisture, and *b* is the latent heat flux. The linear trend was removed over all days, selecting DJF

months only, and across all years to define anomalies relative to the seasonal cycle. We only selected days over the DJF season, between 1950 and 2014. The coupling strength is also computed with a 2-day lag correlation.

3 Interannual and seasonal means

3.1 interannual mean

Observed annual mean precipitation is high over the tropical latitudes, i.e. the Amazon Basin, Colombia and South Venezuela, while northeastern Brazil is relatively dry (Fig. 1a). Precipitation is stronger over the eastern side of the Andes than over the western side, because moisture is carried across South America by the trade easterlies. Over the Andes, peaks in precipitation are collocated with the orography.

HadGEM3 has clear deficiencies in simulating precipitation, particularly over high orography. N96 has a wet bias over southern Brazil and over the Andes, from 30°S to the equator, and a dry bias over northeast Brazil (Fig. 1b). Biases are strong, up to 3 $mm.day^{-1}$ over the Andes. The dry bias over the northeast Brazil is associated with anomalously weak easterlies (Fig. 1b). An anomalously strong cyclonic circulation, located over Peru, weakens the easterlies, between 10°S and the equator, decreasing moisture flux divergence over the western Amazon Basin associated with a wet bias there (Fig. 1b). There is an anomalously strong anticyclonic circulation, over southeast Brazil, which is associated with stronger easterlies from the South Atlantic Ocean to southern Brazil and a wet bias (Fig. 1b).

N216 and N512 also show, wet biases over the Andes and southeastern Brazil, and dry biases over northeast Brazil (Fig. 1c and Fig, 1d). Biases in low-level winds are also very similar in N96, N216 and N512. We highlight the impacts of each step change in resolution by displaying differences between all pairs of simulations. The total impact of shifting from N96 to N512 is given by N512-N96; intermediate steps are illustrated by N216-N96 and N512-N216. This helps to define the minimum resolution required to extract

substantial simulation improvements, from the available sets of simulations. The strongest impact of increasing resolution is over the Andes, where N512-N96 reaches up to 2 $mm.day^{-1}$ (Fig. 2c). Significant differences are also obtained over the Amazon Basin, northeast Brazil and northwest Argentina (Fig. 2a-c). Over the Amazon basin and the Andes, changes in precipitation in N512-N96 are due to both N216-N96 and N512-N216 (Fig. 2a and Fig. 2b). In addition, differences consist of reduced precipitation (Fig. 2abc), and thus in reduced wet biases, over the Andes (Fig. 1bcd; see the stippling). Therefore, it is worth increasing horizontal resolution to N512 for simulating precipitation over the Andes.

Over northern Argentina, significant changes are only due to N216-N96 (Fig. 2a), while there are no significant changes in N512-N216 (Fig. 2b). Over the Amazon Basin, significant changes are found in both N216-N96 and N512-N216. Over the Amazon Basin and northern Argentina, increasing resolution increases precipitation, which strengthens the N96 wet bias. Over northeastern Brazil, the significant increase in precipitation with resolution reduces the N96 dry bias. However, the improvement is primarily found in N216-N96; resolutions higher than N216 do not appear to be useful. Over the Ocean, increased resolution is associated with strong changes in precipitation, i.e. precipitation increases over the eastern Pacific Ocean and decreases over the tropical Atlantic Ocean (especially just offshore of most coastal regions) (Fig. 2), but most of the effect comes from moving from N96 to N216.

Changes in evaporation with resolution are significant over the eastern Pacific Ocean, and over the southwest Atlantic Ocean, along the coast of South America (Fig. 2d-f). However, increasing resolution leads to only moderate changes in evaporation over land. Unlike evaporation, differences in moisture flux convergence (i.e. precipitation minus evaporation) are strong over both land and ocean (Fig. 2g-i). Therefore, the sensitivity of Amazon Basin and Andes precipitation to resolution is mostly due to sensitivity in moisture transport rather than in local moisture recycling (i.e. conversion of local evaporation into precipitation). This is consistent with Vannière et al. (2019), which showed that ocean-to-land moisture advection increases with resolution. We show small changes in specific humidity and surface air

temperature over land (Fig. S1 and Fig. S2). This suggests that changes in precipitation with resolution are due to dynamic changes, rather than thermodynamic changes. Increased resolution is associated with an eastward shift, toward the coast, of the southeast Pacific anticyclonic circulation (Fig. 2g-i) in the southern Pacific coastal region. The wind speed then strengthens and increases evaporation (Fig. 2d-f) and decreases moisture convergence (Fig. 2g-i). Over land, changes in wind speed are particularly strong over the mountains.

3.2 Seasonal means

We next examine the influence of resolution on seasonal rainfall, motivated by the strong seasonal cycle of South American rainfall (i.e., heavy rainfall over northern South America in July-September, while the Amazon basin is wetter in DJF than in JAS). Over northeast Brazil, the resolution sensitivity is strongest in DJF and MAM, mainly due N216-N96 (Fig. 3a; Fig. 3c; Fig. 3d and Fig. 3f), while the N512-N216 differences are moderate (Fig. 3b and Fig. 3e). Differences are also strong over the Amazon Basin, in DJF and SON, where increased resolution increases mean precipitation (Fig. 3c and Fig. 3l). Changes in Amazon Basin precipitation are contributed by both N216-N96 (Fig. 3a and Fig. 3j) and N512-N216 (Fig. 3b and Fig. 3k).

Over southwestern Brazil—northern Argentina, increasing resolution increases precipitation in all seasons which increases the wet bias. These changes are only due to N216-N96 (Fig. 3). Strong differences are also obtained over the tropical Pacific and Atlantic Ocean, from March to November (Fig. 3d, Fig. 3g and Fig. 3j), mainly due to N216-N96. N512-N216 does not strongly affect oceanic precipitation (Fig. 3e, Fig. 3h and Fig. 3k).

Improvements are shown over northeast Brazil in DJF and MAM. There is little sensitivity to resolution elsewhere in South America. Over the Amazon, changes are stronger in austral summer (i.e. DJF), during the monsoon, but biases are higher at high resolution.

4. Seasonal to interannual variability and teleconnections

We have shown a limited effect of resolution on mean precipitation. However, climate variability could be more sensitive to resolution because resolution may affect how the model simulates precipitation distribution, local and large-scale atmospheric dynamics, land-atmosphere coupling and mesoscale systems. Assessing climate variability provides useful information on the ability of climate models to simulate the climate system.

The pattern in annual precipitation variance follows the pattern in annual mean precipitation, i.e. higher along the equator than over the surrounding regions (Fig. 4a). At all resolutions, HadGEM3 overestimates precipitation variability over southeast Brazil, and underestimates precipitation variability between 15°S and the equator (Fig. 4b-d). HadGEM3 overestimates both mean precipitation and precipitation variability over parts of the Andes and southeast Brazil/northern Argentina (Fig. 1b-d and Fig. 4b-d). HadGEM3 has a mean wet bias but underestimates the precipitation variability over the Amazon Basin, although increasing resolution reduces the variability bias (Fig 4.e-g). Over southeast Brazil, increasing resolution slightly reduces the overestimation of precipitation variance (Fig. 4e-g). There are no changes in precipitation variance over northeast Brazil, in N512-N96 (Fig. 4e, Fig. 4f and Fig. 4g).

Precipitation variance also increases with resolution for individual seasons (not shown). Because both Pacific and Atlantic SSTs affect seasonal-to-interannual South American precipitation variability, we hypothesized that changes in variance to be associated with a change in the strength of the teleconnection between ENSO and South American precipitation, and between the South Atlantic SSTs and South American precipitation. However, this hypothesis was not supported by the following evidences: The

297 impact of ENSO on South America is assessed through regressing the El Niño 3.4 index (170-120°W; 5°S-
298 5°N) onto precipitation for each grid point, focusing on the seasonal anomalies (Fig. S3). We found that
299 increasing horizontal resolution does not systematically alter the influence of ENSO on Brazilian
300 precipitation. These analyses were repeated, focusing on tropical Atlantic gradients in SST, yielding a
301 similar conclusion to the one for ENSO, i.e. increasing the horizontal resolution does not change impacts
302 of the SST on precipitation over land (not shown).
303

5. Daily to sub-seasonal variability and teleconnections

5.1 Daily variability

Daily precipitation variance is more sensitive to resolution that monthly or annual variance. Over the Amazon Basin, differences between the simulations are stronger in austral summer than other seasons (Fig. S4). Besides, precipitation variability is strongly tied to the South American summer monsoon, which mainly occurs in DJF. Therefore, we focus further analysis on daily variance and on DJF.

In DJF, N96 underestimates daily precipitation variance (Fig. 5a). N216 and N512 outperform N96, with a reduced underestimation of precipitation variance over the Amazon Basin (Fig. 5b and Fig. 5c). The increase in variance is due to shifts from N96 to N216 and N216 to N512 (Fig. 5d and Fig. 5e). The difference in P-E variance is high, close to the difference in P variance (Fig. 5g; Fig. 5h and Fig. 5i). Therefore, changes in precipitation variance are mostly associated with changes in the variance of moisture flux convergence.

Biases in DJF daily precipitation variance have also been assessed using CMORPH over 1998-2014. The same conclusions are drawn: N96 underestimates variance and N512 overestimates variance (Fig. S4). However, the N96 biases are much reduced when compared to CMORPH instead of GPCC, such that N96 outperforms N216 and N512 (Fig. S4 and Fig. S5). In addition, the northern Brazil circulation is dominated by easterlies (Fig. 1a), whose variability reinforces by increasing the horizontal resolution (Fig. S6). Over southern Brazil, the circulation is dominated by northerlies; increasing resolution increases meridional wind variance (Fig. S7). Therefore, we suggest the change in precipitation variance is associated with changes in atmospheric dynamics. A positive feedback exists since an increase in precipitation is associated with a strengthening of local vertical velocity, which strengthens the low-level wind. However, changes in wind variance exhibit a large-scale pattern that suggests changes that are not due solely to local precipitation increases. The variance of the meridional wind increases strongly over the eastern side of the Andes (Fig. S7), highlighting the importance of the orography in modulating the circulation and transporting moisture.

We analyzed the variance of the zonal and meridional components of the moisture flux and found the same patterns as for the low-level wind (not shown), suggesting that changes are mostly attributed to dynamic changes, rather than thermodynamic changes.

5.2 Effects of the Madden-Julian Oscillation

The Madden Julian Oscillation (MJO) strongly affects sub-seasonal precipitation variability over Brazil (Grimm, 2019; Grimm and Silva Dias, 1995; Grimm and Tedeschi, 2009; Lewis et al., 2011; Marengo et al., 2008, 2011, 2013). Therefore, a change in the MJO teleconnection to South America may alter precipitation mean and variance.

Indices of the Madden-Julian Oscillation (MJO) have been computed using NCEP for observed wind and outgoing longwave radiation from NOAA Cooperative Institute for Research in Environmental Sciences data set (Liebmann and Smith, 1996), following Wheeler and Hendon (2004), by computing empirical orthogonal functions on daily values of 850 and 200 hPa zonal winds and outgoing longwave radiation. Simulated MJO indices are performed by projecting model data onto the reanalysis EOFs, after first removing the model annual mean and the first three harmonics of the model annual cycle. MJO indices were computed on data first interpolated on a 2.5° resolution. See Wheeler and Hendon (2004) for a longer description of the method. Time series have been deseasonalised and linearly detrended prior to computing impacts of MJO on precipitation mean and variance.

In observations (GPCC), the MJO strongly impacts tropical South American precipitation, leading to above average precipitation during phases 1 and 8, while phases 3, 4 and 5 are associated with anomalously dry conditions (Fig. 6, top two rows), as shown in Grimm (2019). South of 20°S, phases 1, 7 and 8 are associated with anomalously dry conditions and phases 3, 4 and 5 with anomalously wet conditions (Fig. 6, top panel). We select two areas, the Amazon Basin, where differences in precipitation variance between simulations are strong and East Brazil, which is strongly impacted by the MJO. Note the boxes on Fig. 6a. Both areas

experience above average precipitation during MJO phases 1, 7 and 8, and below average precipitation during phases 3, 4 and 5 (Fig. 6a-b). HadGEM3 reproduces the impact of MJO on East Brazil and Amazon Basin precipitation in sign and magnitude (Fig. 6i-j). There are no clear differences between N96, N216 and N512 simulations, and an impact of the horizontal resolution does not emerge.

We show strong impacts of resolution on precipitation variance in Sect. 5.1. Therefore, we address here how precipitation variance could be affected by resolution within each MJO phase. Results are given relative to the variance of the precipitation computed from the full original daily timeseries (with no selection of any specific MJO phases). Results for precipitation variance differ slightly from those for the mean precipitation, with for instance a decrease in the variance during phase 1 when mean precipitation is higher, and stronger during phase 3 when mean precipitation is lower. This difference could also arise from local differences that could strongly impact the area-average. HadGEM3 simulates well the impact of the MJO on the precipitation variance, with above average variance during phases 7 and 8 and below average variance during phases 4 and 5. Unlike the observation, HadGEM3 simulates an increase in the variance of the precipitation during phase 1 of the MJO. N216 and N512 simulations perform better than N96 for phase 3 of the MJO, since the N96 simulates reduced precipitation variance while the variance is anomalously high in observation and in the N512 and N216 simulations. However, there is no clear sensitivity of MJO-related precipitation variance to horizontal resolution.

5.3 Land-atmosphere feedback

Soil moisture memory contributes to atmospheric variability and could potentially affect the development of the South American Monsoon System. Land-atmosphere coupling is particularly strong over South America (Koster et al., 2004; Sörensson and Menéndez, 2011). In this section we assess the sensitivity of land-atmosphere feedbacks to resolution, using ERA-interim as verifying “observations”. The coupling

strength metric is defined as the correlation between two variables, weighted by the standard deviation of the reference variable (see Sect. 2.4).

Over the Amazon Basin, there is a positive relationship between observed precipitation and observed soil moisture (Fig. 7a), such that an increase in precipitation is associated with anomalously high soil moisture, with soil moisture are coincident with changes in precipitation (Fig. 7e). Over the Amazon Basin and in all HadGEM3 resolutions, the bias in the precipitation—soil moisture coupling strength is small (Fig. 7b-d) and increase in the resolution does not change precipitation—soil moisture coupling strength (Fig. 7i-k; Fig. 7l-n), probably because, over the Amazon, the soil is saturated, such that increases in precipitation variability do not impact soil moisture variability. Soil moisture and evaporation are negatively correlated in observations, such that increased evaporation decreases soil moisture, over the Amazon Basin (Fig. 8a). Over the Amazon Basin, there is not a strong lead-lag relationship between soil moisture and evaporation in observations (Fig. 8e) or in HadGEM3 (Fig, 8f-h). The coupling strength is overestimated in N96 (Fig. 8b) but an increase in resolution reduces this overestimation (Fig. 8c-d and Fig.8f-g). Over the Amazon Basin, the moisture budget is energy-limited, rather than moisture limited (Cook et al., 2014). Therefore, we also assessed the coupling strength between temperature and evaporation. An increase in temperature is associated with increased evaporation (Fig. S8) and thus decreased soil moisture, but, in HadGEM3, this coupling strength is not sensitive to resolution (Fig. S8). These results are consistent with our previous results, showing that local recycling plays a moderate role in explaining changes in precipitation variance, which is mainly associated with change in the moisture flux convergence variability (Fig. 6), rather than with a stronger land-atmosphere coupling (Fig. 8).

Outside of the Amazon Basin, the soil moisture-precipitation relationship is positive in both observations (Fig. 7a) and HadGEM3 (Fig. 7b-d), with precipitation variability leading soil moisture variability (Fig. 7b and Fig. 7f-h). The increase in soil moisture increases evaporation over eastern Brazil (Fig. 8a). The soil moisture—evaporation coupling strength is too high in all simulations over northeastern and eastern Brazil (Fig. 8b-d), with soil moisture driving evaporation, because evaporation is moisture-limited over northeast

Brazil, with changes in evaporation leading changes in temperature (Fig. S8). The strengths of both precipitation—soil moisture and soil moisture—evaporation couplings are overestimated in N96 (Fig. 7b and Fig.8b) over eastern Brazil and southeastern South America. Increasing resolution reduces this overestimation (Fig. 7cd; Fig. 7i-k; Fig. 8cd; Fig, 8i-k).

5.4 Scales of precipitation

We use the ASoP diagnostics (see section 2.4) to assess daily precipitation features over South America in HadGEM3, and verify them against CMORPH. We compute the fractional contribution to total CMORPH precipitation from four precipitation intensity bins, over South America, with a focus over two sub-regions, the Amazon Basin (AMZ) and southeast South America (SESA). We compare spatial and temporal scales of precipitation features across datasets for the two subregions. Results are given, separately, for light, moderate and heavy rainfall events. We focus on the occurrence and duration of dry spells.

5.4.1 Light precipitation and dry spells

In CMORPH, light precipitation events (<10 $mm.day^{-1}$) contribute the most of all intensity categories to total precipitation over most of the Andes and northern and southern South America, the Pacific Ocean and western Atlantic Ocean (Fig. 9a). N96 underestimates contributions from light precipitation events over the Andes and southeast Brazil, but overestimates contributions from light precipitation over the Amazon Basin and northeastern Brazil (Fig. 9e). The results are consistent with Seth et al. (2004), which also show an overestimation of the percentage of light rain events over South America. This bias is reduced by increasing resolution to N216 and N512 (Fig, 9i-p; Fig. S9).

Figure 10 shows frequencies of precipitation events, as classified by intensity and duration. Results are shown for two regions: AMZ, where variance is too weak; and SESA, where variance is too high. Over

AMZ and SESA, near-zero precipitation (rainy events of 0.1 – 1 mm.day^{-1}) can last for more than 15 days, while events of 1 – 10 mm.day^{-1} can last for up to 4 or 5 days (Fig. 10a and Fig. 10f). Over AMZ, N96 overestimates the frequency of events of 2 to 12 mm.day^{-1} and underestimates the frequency of those of less than 1 mm.day^{-1}, compared to CMORPH (Fig. 10b). For SESA, N96 underestimates the frequency of precipitation events of less than 1 mm.day^{-1} and lasting between 1 and 8 days; the model overestimates the frequency of near-zero rainy days, lasting more than 8 days (Fig. 10g). Intensity-duration biases improve with resolution over AMZ (Fig. 10c-10d) and SESA (Fig. 10h-10i). However, the biases worsen with resolution for near-zero precipitation lasting for any duration over AMZ, and for intensities between 1-9 mm.day^{-1} with a duration of 1-5 days over SESA.

In addition to events of less than 10 mm.day^{-1}, we assess simulated frequency and duration of dry spells, defined by events of less than 0.1 mm.day^{-1}. We create 2-D histograms for duration versus frequency of dry days over AMZ and SESA (Fig. 11). CMORPH shows more frequent short-duration dry spells as compared to HadGEM3 over AMZ at both native (Fig. 11a) and N96 (Fig. 11c) resolutions. Over SESA, CMORPH also generally shows more frequent dry spells for durations longer than 1 day (Fig. 11b, 11d). The sensitivity of dry-spell frequency to model resolution is generally smaller than the model bias. Once all datasets are interpolated to the common N96 resolution, N96 produces longer and more frequent dry spells than N216 and N512, and is closer to CMORPH.

5.4.2 Moderate precipitation

Over most other parts of South America (i.e. Amazon and central and eastern Brazil), most of the total precipitation is contributed by light to moderate events (10-40 mm.day^{-1}; Fig. 9a-c). Compared to CMORPH, N96 overestimates the contribution from moderate events, to total precipitation, over the Andes and underestimates this contribution over South America outside of the Andes (Fig. 9f, 9g). Although the spatial pattern of biases is similar to N96, biases in contribution from moderate rainfall to total precipitation reduce when increasing resolution (Fig. 9f-j-n and Fig. 9g-k-o; Fig. S9).

Over AMZ and SESA, most precipitation comes from moderate events in both CMORPH and HadGEM3 (Fig. 10b-e). Over AMZ, CMORPH distribution peaks at ~30 mm.day^{-1} (Fig. 10b, 10d), when using the CMORPH native grid (Fig. 10b), and at ~20 mm.day^{-1} when using the N96 grid (Fig. 10d). At their native resolutions, N96, N216 and N512 have a primary peak at ~9 mm.day^{-1} and a secondary peak at ~30 mm.day^{-1} (Fig. 10b). On the N96 grid, the secondary peak is removed in N216 and N512. As the fractional contribution in HadGEM3 peaks at lower intensities for all three resolutions, HadGEM3 overestimates the contribution from intensities below ~15 mm.day^{-1} and underestimates contribution from intensities above 15 mm.day^{-1} (Fig. 10b). When compared on their native grids, the model biases reduce with resolution over AMZ. However, once interpolated to N96, N512 has the largest bias in fractional contribution, around the peak intensity (i.e. at ~10 mm.day^{-1}). Over AMZ, N96 underestimates the frequency of events of 12-40 mm.day^{-1} (Fig. 10d and Fig. 12b). Increasing resolution reduces the biases for the frequency of events of 12-25 mm.day^{-1} but leads to an underestimation of precipitation of 30 to 40 mm.day^{-1} (Fig. 10b and Fig. 12c-e). Over SESA, distribution peaks at ~20-30 mm.day^{-1} (Fig. 12c and Fig. 12e). Over SESA, N96 underestimates (overestimates) the frequency of events of 2-20 mm.day^{-1} (20-40 mm.day^{-1}) (Fig. 10g; Fig. 12e). These biases are reduced in at N216 and N512 (Fig. 10h-j; Fig. 12e).

5.4.3 Heavy precipitation

Parts of the Peruvian Andes, Uruguay and northeastern Argentina receive most of their rainfall from heavy events (>40 mm.day^{-1}; Fig. 9d). N96 overestimates these contributions (>40 mm.day^{-1}) over central Brazil, the eastern Amazon and southeastern Brazil (Fig. 9h). Like for the light and moderate events, increasing resolution reduces these biases (Fig. 9h-p and Fig. S9). This suggests that, at higher resolution, HadGEM3 performs better for the frequency of extreme events, such as those that lead to flooding. However, the improvements primarily come from the increase from N96 to N216, not from N216 to N512 (Fig. S9). In addition, N96 overestimates the frequency of events > 40 mm.day^{-1} over AMZ and SESA (Fig. 10b; Fig. 10g). Increasing resolution reduces these biases, again mostly due to increase from the N96 to N216

resolution, not from N216 to N512. For AMZ, N512 has a higher bias than N216 for events of 40-90 $mm.day^{-1}$.

5.4.4 Temporal and spatial scales

To compare spatial and temporal scales of precipitation features across datasets, we plot correlations as functions of distance (Fig. 13a-d) and time (Fig. 13e-h) (see section 2.4). Over AMZ, N96 overestimates the spatial and temporal scales of precipitation events relative to CMORPH, on their native grids (Fig. 13a and Fig. 13e). However, once CMORPH is interpolated to the N96 grid, N96 simulation underestimates the spatial scale (and overestimates the temporal scale) of precipitation (Fig 13b and Fig. 13f), highlighting that results strongly depend on the analysis grid. For SESA, N96 also underestimates the spatial scale and overestimates temporal scale of precipitation (Fig. 13d-g-h). When considering native grids only, there are no clear differences between N96 and CMORPH for the spatial extent of precipitation events (Fig. 13c).

On native grids, N96 simulates events with larger spatial scales than N216 and N512 (Fig. 13a). However, this is mainly due to the coarse N96 grid. While all datasets are interpolated onto the N96 grid, N96 events are smaller than those in N216 and N512, which show similar scales and are closer to CMORPH (Fig. 13b). Over SESA, spatial scales are similar in all simulations, on their native grids (Fig. 13c). However, as for AMZ, at N96 resolution N512 and N216 are closer to CMORPH than to N96 (Fig. 13d). For both AMZ and SESA, therefore, the spatial features of daily precipitation events are better simulated at higher resolution.

At all resolutions, simulated precipitation features persist longer than in CMORPH (Fig. 13e-h). Over AMZ and SESA, biases are lowest in N96, which simulates events that are less persistent than in N216 and N512 (Fig. 13f, Fig. 13h). This bias increases at higher resolution. Therefore, increasing horizontal resolution does not improve biases in temporal scales of precipitation.

6 Conclusion

We assess the effects of increasing horizontal resolution on simulated South American precipitation. We use atmosphere-only simulations, performed with HadGEM3-GC3.1 (Williams et al., 2018) at three horizontal resolutions: N96 (~130 km, 1.88° x 1.25), N216 (~60 km, 0.83° × 0.56°), and N512 (~25 km, 0.35° x 0.23°). We assess, systematically, how the step change between each resolution effects simulated precipitation, focusing on precipitation mean and variance, and on fine scale processes, such as temporal and spatial scales, frequency of heavy and light precipitation events and dry-spell durations.

We show that the atmosphere-only simulations have systematic biases in simulating annual mean and seasonal mean precipitation over South America. Northeast Brazil is anomalously dry, while the southeast Brazil and the Andes are too wet. These biases are mostly due to atmospheric circulation biases: underestimated trade easterlies, and a displaced anticyclonic circulation over southeast Brazil, both acting to modify moisture transport over South America. Increasing horizontal resolution affects the simulated precipitation. For instance, precipitation biases reduce over the Andes and over northeast Brazil. It is worth increasing the resolution to N512 (~25 km) for simulating precipitation over the Andes Mountains. This is consistent with Vannière et al. (2019), which shows that the added value of increasing horizontal resolution is greatest over orography. Over northeast Brazil, the largest improvement comes from increasing resolution to N216 (~60 km); a further increase to N512 is only associated with moderate changes. Increasing resolution does not improve model biases over the Amazon Basin. These results are consistent with Roberts et al. (2018) for the Amazon Basin and northeast and south Brazil. In addition, improvements vary seasonally: changes are the strongest over northeast Brazil in DJF and MAM, when precipitation is also highest. Over the Andes, the results are similar in all seasons.

Biases in mean precipitation are collocated with biases in regional precipitation variance. For instance, northeast Brazil is too dry and HadGEM3-GC3.1 systematically underestimates precipitation variance,

525 while southeast Brazil is too wet and HadGEM3-GC3.1 systematically overestimates precipitation
526 variance. However, this does not hold for the Amazon Basin, which is too wet but where the precipitation
527 variance is strongly underestimated. Precipitation variance is stronger at daily scales than at monthly scales;
528 biases are strongest in DJF and over the Amazon Basin. Increasing resolution increases precipitation
529 variance, hence reducing biases. The increase in precipitation variance is associated with an increase in
530 moisture flux convergence variance over land, and with changes in the variance of the low-level winds;
531 local recycling of evaporation has a limited role. Relatedly, coupling strengths between evaporation, soil
532 moisture and precipitation are only weakly sensitive to resolution, except for some improvements in
533 coupling strength over eastern and southeastern Brazil. We found only modest sensitivity to resolution for
534 the teleconnections of the El-Niño Southern Oscillation and Madden-Julian Oscillation to land
535 precipitation. This suggests that changes in precipitation mean and variance are not due to changes in these
536 teleconnections.
537
538 HadGEM3-GC3.1 has biases in its precipitation distribution. For instance, the model does not produce
539 enough dry days over the Amazon Basin or moderate rain days (10-40 $mm.day^{-1}$), while simulating too
540 many light events (<10 $mm.day^{-1}$) and heavy events (>40 $mm.day^{-1}$). Over southeast Brazil, the model
541 simulates too few short dry spells and too many long ones. HadGEM3-GC3.1 simulates too few and too
542 short events of 2 to 16 $mm.day^{-1}$, but simulates too many and too long events of more than 20 $mm.day^{-1}$.
543 These metrics are important for understanding the ability of climate models to simulate high-impact events.
544 Increasing resolution reduces these biases; N512 is therefore better at simulating precipitation distributions
545 than N96. In addition, increasing the horizontal resolution increases the spatial scale of daily rain events,
546 suggesting a better simulation of organised mesoscale systems. However, the persistence of precipitation
547 events is better simulated at N96, showing no clear sensitivity to resolution. Other models also overestimate
548 light events at the expense of heavy events over the Amazon and eastern Brazil, and overestimate heavy
549 events at the expense of lighter ones in southeast Brazil (Seth et al., 2004).
550

Over South America, precipitation results from the combination of the predominant role played by the InterTropical Convergence Zone and the South Atlantic Convergence Zone (Liebmann et al., 1999; Waliser et al., 1993). In addition, mesoscale systems such as squall lines may be responsible for a large fraction of Amazonian precipitation (Cohen et al., 1995). Our results show that increasing the horizontal resolution increases the spatial scale of rain events, i.e. of the mesoscale systems, over both Amazonia and southeast Brazil. Therefore, we speculate that increasing resolution could lead to more organized convective systems, which would be consistent with the increase in moisture flux convergence, as shown over South America at the highest resolution. This would be consistent with Vellinga et al. (2016) who showed that N512 resolution improved mesoscale systems over West Africa relative to N96 or N216. Conversely, the decrease in the persistence of such events (highest at the N96 resolution) could be associated with an increase in daily rainfall variability, because of less persistent rainy events. Those are hypotheses that should be assessed in more detail in a specific study, potentially with models at sufficiently high resolution to disable convective parameterisations.

Although we hypothesized that increasing resolution might affect the ability of climate models to predict precipitation, Bombardi et al. (2018) have shown that an improvement of South American precipitation prediction due to an increase in resolution is not straightforward. In addition to resolution, further works should, therefore, be devoted to understanding the effects of physic, on prediction system performance.

The mechanism for increases in precipitation variance with resolution are still unclear. The increase in precipitation variance is a global feature, not limited to South America (Fig. S10). Further work is needed to understand better this behavior at global scale. Besides, we used AMIP-type simulations; and results could be different in coupled models, in which the ocean can interact with atmospheric variability, particularly when accounting for SST teleconnections.

Code availability. Codes used to perform analysis and figures are publicly available at https://doi.org/10.5281/zenodo.3840095. For the analysis of the scales of precipitation (ASoP), codes are available on https://github.com/nick-klingaman/dubstep/tree/master/asop, https://github.com/nick-klingaman/dubstep/tree/master/asop_duration, and https://zenodo.org/record/3997114#.X0PGrjV7mUk.

Data availability. The model data used in the analysis are available from the CMIP6 Earth System Grid Federation, for N96 (HadGEM3-GC31-LM; https://doi.org/ 10.22033/ESGF/CMIP6.1321), N216 (HadGEM3-GC31-MM; https://doi.org/ 10.22033/ESGF/CMIP6.1902) and N512 (HadGEM3-GC31-HM; https://doi.org/ 10.22033/ESGF/CMIP6.446). The list of persistent identifiers of the data we have used is available at **https://doi.org/10.5281/zenodo.3840095**

Author contributions. AC, PAM and PC performed the data analysis. PAM prepared the manuscript with contributions from all co-authors.

Acknowledgements

This work was supported by the Newton Fund through the Met Office Climate Science for Service Partnership Brazil (CSSP Brazil). NPK was funded by an Independent Research Fellowship from the Natural Environment Research Council (NE/L010976/1) and by the NERC/GCRF programme Atmospheric hazard in developing countries: risk assessment and early warnings (ACREW). Detailed calculations and code for the ASoP diagnostics are available at https://github.com/achevuturi/asop_duration. NOAA OLR data can be obtained from the website (https://www.esrl.noaa.gov/psd/data/gridded/data.interp_OLR.html). Authors thank Dr. Pier Luigi Vidale for his insightful and constructive comments. The authors thank the two anonymous reviewers for their constructive comments and suggestions.

References

Bacmeister, J. T., Wehner, M. F., Neale, R. B., Gettelman, A., Hannay, C., Lauritzen, P. H., Caron, J. M. and Truesdale, J. E.: Exploratory High-Resolution Climate Simulations using the Community Atmosphere Model (CAM), J. Clim., 27(9), 3073–3099, doi:10.1175/JCLI-D-13-00387.1, 2013.

Bombardi, R. J. and Carvalho, L. M. V: IPCC global coupled model simulations of the South America monsoon system, Clim. Dyn., 33(7), 893, doi:10.1007/s00382-008-0488-1, 2008.

Bombardi, R. J., Trenary, L., Pegion, K., Cash, B., DelSole, T. and Kinter III, J. L.: Seasonal Predictability of Summer Rainfall over South America, J. Clim., 31(20), 8181–8195, doi:10.1175/JCLI-D-18-0191.1, 2018.

Coelho, C. A. S., de Oliveira, C. P., Ambrizzi, T., Reboita, M. S., Carpenedo, C. B., Campos, J. L. P. S., Tomaziello, A. C. N., Pampuch, L. A., Custódio, M. de S., Dutra, L. M. M., Da Rocha, R. P. and Rehbein, A.: The 2014 southeast Brazil austral summer drought: regional scale mechanisms and teleconnections, Clim. Dyn., 46(11), 3737–3752, doi:10.1007/s00382-015-2800-1, 2016.

Cohen, J. C. P., Silva Dias, M. A. F. and Nobre, C. A.: Environmental Conditions Associated with Amazonian Squall Lines: A Case Study, Mon. Weather Rev., 123(11), 3163–3174, doi:10.1175/1520-0493(1995)123<3163:ECAWAS>2.0.CO;2, 1995.

Cook, B. I., Smerdon, J. E., Seager, R. and Coats, S.: Global warming and 21st century drying, Clim. Dyn., 43(9), 2607–2627, doi:10.1007/s00382-014-2075-y, 2014.

Custodio, M. de S., da Rocha, R. P., Ambrizzi, T., Vidale, P. L. and Demory, M.-E.: Impact of increased horizontal resolution in coupled and atmosphere-only models of the HadGEM1 family upon the climate patterns of South America, Clim. Dyn., 48(9), 3341–3364, doi:10.1007/s00382-016-3271-8, 2017.

Custódio, M. de S., Porfírio da Rocha, R. and Vidale, P. L.: Analysis of precipitation climatology simulated by high resolution coupled global models over the South America, Hydrol. Res. Lett., 6, 92–97, doi:10.3178/hrl.6.92, 2012.

Dai, A.: Precipitation Characteristics in Eighteen Coupled Climate Models, J. Clim., 19(18), 4605–4630, doi:10.1175/JCLI3884.1, 2006.

Dee, D. P., Uppala, S. M., Simmons, A. J., Berrisford, P., Poli, P., Kobayashi, S., Andrae, U., Balmaseda, M. A., Balsamo, G., Bauer, P., Bechtold, P., Beljaars, A. C. M., van de Berg, L., Bidlot, J., Bormann, N., Delsol, C., Dragani, R., Fuentes, M., Geer, A. J., Haimberger, L., Healy, S. B., Hersbach, H., Hólm, E. V, Isaksen, L., Kållberg, P., Köhler, M., Matricardi, M., McNally, A. P., Monge-Sanz, B. M., Morcrette, J.-J., Park, B.-K., Peubey, C., de Rosnay, P., Tavolato, C., Thépaut, J.-N. and Vitart, F.: The ERA-Interim reanalysis: configuration and performance of the data assimilation system, Q. J. R. Meteorol. Soc., 137(656), 553–597, doi:10.1002/qj.828, 2011.

DelSole, T. and Shukla, J.: Model Fidelity versus Skill in Seasonal Forecasting, J. Clim., 23(18), 4794–4806, doi:10.1175/2010JCLI3164.1, 2010.

Delworth, T. L., Rosati, A., Anderson, W., Adcroft, A. J., Balaji, V., Benson, R., Dixon, K., Griffies, S. M., Lee, H.-C., Pacanowski, R. C., Vecchi, G. A., Wittenberg, A. T., Zeng, F. and Zhang, R.: Simulated Climate and Climate Change in the GFDL CM2.5 High-Resolution Coupled Climate Model, J. Clim., 25(8), 2755–2781, doi:10.1175/JCLI-D-11-00316.1, 2011.

Demory, M.-E., Vidale, P. L., Roberts, M. J., Berrisford, P., Strachan, J., Schiemann, R. and Mizielinski, M. S.: The role of horizontal resolution in simulating drivers of the global hydrological cycle, Clim. Dyn., 42(7), 2201–2225, doi:10.1007/s00382-013-1924-4, 2014.

Doblas-Reyes, F. J., Andreu-Burillo, I., Chikamoto, Y., García-Serrano, J., Guemas, V., Kimoto, M., Mochizuki, T., Rodrigues, L. R. L. and van Oldenborgh, G. J.: Initialized near-term regional climate change prediction, Nat. Commun., 4, 1715, doi:10.1038/ncomms2704, 2013.

Falco, M., Carril, A. F., Menéndez, C. G., Zaninelli, P. G. and Li, L. Z. X.: Assessment of CORDEX simulations over South America: added value on seasonal climatology and resolution considerations, Clim. Dyn., 52(7), 4771–4786, doi:10.1007/s00382-018-4412-z, 2019.

Gent, P. R., Yeager, S. G., Neale, R. B., Levis, S. and Bailey, D. A.: Improvements in a half degree atmosphere/land version of the CCSM, Clim. Dyn., 34(6), 819–833, doi:10.1007/s00382-009-0614-8, 2010.

Grimm, A. M.: Madden--Julian Oscillation impacts on South American summer monsoon season: precipitation anomalies, extreme events, teleconnections, and role in the MJO cycle, Clim. Dyn., doi:10.1007/s00382-019-04622-6, 2019.

Grimm, A. M. and Silva Dias, P. L.: Analysis of Tropical–Extratropical Interactions with Influence Functions of a Barotropic Model, J. Atmos. Sci., 52(20), 3538–3555, doi:10.1175/1520-0469(1995)052<3538:AOTIWI>2.0.CO;2, 1995.

Grimm, A. M. and Tedeschi, R. G.: ENSO and Extreme Rainfall Events in South America, J. Clim., 22(7), 1589–1609, doi:10.1175/2008JCLI2429.1, 2009.

Haarsma, R. J., Roberts, M. J., Vidale, P. L., Senior, C. A., Bellucci, A., Bao, Q., Chang, P., Corti, S., Fučkar, N. S. and Guemas, V.: High resolution model intercomparison project (HighResMIP v1. 0) for CMIP6, Geosci. Model Dev., 9(11), 4185–4208, 2016.

Jia, L., Yang, X., Vecchi, G. A., Gudgel, R. G., Delworth, T. L., Rosati, A., Stern, W. F., Wittenberg, A. T., Krishnamurthy, L., Zhang, S., Msadek, R., Kapnick, S., Underwood, S., Zeng, F., Anderson, W. G., Balaji, V. and Dixon, K.: Improved Seasonal Prediction of Temperature and Precipitation over Land in a High-Resolution GFDL Climate Model, J. Clim., 28(5), 2044–2062, doi:10.1175/JCLI-D-14-00112.1, 2014.

Joyce, R. J., Janowiak, J. E., Arkin, P. A. and Xie, P.: CMORPH: A Method that Produces Global Precipitation Estimates from Passive Microwave and Infrared Data at High Spatial and Temporal Resolution, J. Hydrometeorol., 5(3), 487–503, doi:10.1175/1525-7541(2004)005<0487:CAMTPG>2.0.CO;2, 2004.

Jung, T., Miller, M. J., Palmer, T. N., Towers, P., Wedi, N., Achuthavarier, D., Adams, J. M., Altshuler, E. L., Cash, B. A., Kinter, J. L., Marx, L., Stan, C. and Hodges, K. I.: High-Resolution Global Climate Simulations with the ECMWF Model in Project Athena: Experimental Design, Model Climate, and Seasonal Forecast Skill, J. Clim., 25(9), 3155–3172, doi:10.1175/JCLI-D-11-00265.1, 2011.

Kanamitsu, M., Ebisuzaki, W., Woollen, J., Yang, S.-K., Hnilo, J. J., Fiorino, M., Potter, G. L., Kanamitsu, M., Ebisuzaki, W., Woollen, J., Yang, S.-K., Hnilo, J. J., Fiorino, M. and Potter, G. L.: NCEP–DOE AMIP-II Reanalysis (R-2), Bull. Am. Meteorol. Soc., 83(11), 1631–1643, doi:10.1175/BAMS-83-11-1631, 2002.

687 Kirtman, B. P., Bitz, C., Bryan, F., Collins, W., Dennis, J., Hearn, N., Kinter, J. L., Loft, R., Rousset, C.,
688 Siqueira, L., Stan, C., Tomas, R. and Vertenstein, M.: Impact of ocean model resolution on CCSM
689 climate simulations, Clim. Dyn., 39(6), 1303–1328, doi:10.1007/s00382-012-1500-3, 2012.

690 Klingaman, N. P., Martin, G. M. and Moise, A.: ASoP (v1.0): a set of methods for analyzing scales of
691 precipitation in general circulation models, Geosci. Model Dev., 10(1), 57–83, doi:10.5194/gmd-10-57-
692 2017, 2017.

693 Knight, J. R., Folland, C. K. and Scaife, A. A.: Climate impacts of the Atlantic Multidecadal Oscillation,
694 Geophys. Res. Lett., 33(17), L17706, doi:10.1029/2006GL026242, 2006.

695 Koster, R. D., Dirmeyer, P. A., Guo, Z., Bonan, G., Chan, E., Cox, P., Gordon, C. T., Kanae, S.,
696 Kowalczyk, E., Lawrence, D., Liu, P., Lu, C.-H., Malyshev, S., McAvaney, B., Mitchell, K., Mocko, D.,
697 Oki, T., Oleson, K., Pitman, A., Sud, Y. C., Taylor, C. M., Verseghy, D., Vasic, R., Xue, Y. and Yamada,
698 T.: Regions of Strong Coupling Between Soil Moisture and Precipitation, Science (80-.)., 305(5687),
699 1138 LP – 1140, doi:10.1126/science.1100217, 2004.

700 Koutroulis, A. G., Grillakis, M. G., Tsanis, I. K. and Papadimitriou, L.: Evaluation of precipitation and
701 temperature simulation performance of the CMIP3 and CMIP5 historical experiments, Clim. Dyn., 47(5),
702 1881–1898, doi:10.1007/s00382-015-2938-x, 2016.

703 Lewis, S. L., Brando, P. M., Phillips, O. L., van der Heijden, G. M. F. and Nepstad, D.: The 2010
704 Amazon Drought, Science (80-.)., 331(6017), 554 LP – 554, doi:10.1126/science.1200807, 2011.

705 Liebmann, B. and Smith, C. A.: Description of a Complete (Interpolated) Outgoing Longwave Radiation
706 Dataset, Bull. Am. Meteorol. Soc., 77(6), 1275–1277 [online] Available from:
707 http://www.jstor.org/stable/26233278, 1996.

708 Liebmann, B., Kiladis, G. N., Marengo, J., Ambrizzi, T. and Glick, J. D.: Submonthly Convective
709 Variability over South America and the South Atlantic Convergence Zone, J. Clim., 12(7), 1877–1891,
710 doi:10.1175/1520-0442(1999)012<1877:SCVOSA>2.0.CO;2, 1999.

711 Liu, W. T. and Juárez, R. I. N.: ENSO drought onset prediction in northeast Brazil using NDVI, Int. J.
712 Remote Sens., 22(17), 3483–3501, doi:10.1080/01431160010006430, 2001.

713 Marengo, J. A., Nobre, C. A., Tomasella, J., Oyama, M. D., Sampaio de Oliveira, G., de Oliveira, R.,
714 Camargo, H., Alves, L. M. and Brown, I. F.: The Drought of Amazonia in 2005, J. Clim., 21(3), 495–516,
715 doi:10.1175/2007JCLI1600.1, 2008.

716 Marengo, J. A., Tomasella, J., Alves, L. M., Soares, W. R. and Rodriguez, D. A.: The drought of 2010 in
717 the context of historical droughts in the Amazon region, Geophys. Res. Lett., 38(12),
718 doi:doi:10.1029/2011GL047436, 2011.

719 Marengo, J. A., Alves, L. M., Soares, W. R., Rodriguez, D. A., Camargo, H., Riveros, M. P. and Pabló,
720 A. D.: Two Contrasting Severe Seasonal Extremes in Tropical South America in 2012: Flood in
721 Amazonia and Drought in Northeast Brazil, J. Clim., 26(22), 9137–9154, doi:10.1175/JCLI-D-12-
722 00642.1, 2013.

723 Martin, G. M., Klingaman, N. P. and Moise, A. F.: Connecting spatial and temporal scales of tropical
724 precipitation in observations and the MetUM-GA6, Geosci. Model Dev., 10(1), 105–126,
725 doi:10.5194/gmd-10-105-2017, 2017.

McClean, J. L., Bader, D. C., Bryan, F. O., Maltrud, M. E., Dennis, J. M., Mirin, A. A., Jones, P. W., Kim, Y. Y., Ivanova, D. P., Vertenstein, M., Boyle, J. S., Jacob, R. L., Norton, N., Craig, A. and Worley, P. H.: A prototype two-decade fully-coupled fine-resolution CCSM simulation, Ocean Model., 39(1), 10–30, doi:https://doi.org/10.1016/j.ocemod.2011.02.011, 2011.

Power, S., Casey, T., Folland, C., Colman, A. and Mehta, V.: Inter-decadal modulation of the impact of ENSO on Australia, Clim. Dyn., 15(5), 319–324, doi:10.1007/s003820050284, 1999.

Rayner, N. A., Brohan, P., Parker, D. E., Folland, C. K., Kennedy, J. J., Vanicek, M., Ansell, T. J. and Tett, S. F. B.: Improved Analyses of Changes and Uncertainties in Sea Surface Temperature Measured In Situ since the Mid-Nineteenth Century: The HadSST2 Dataset, J. Clim., 19(3), 446–469, doi:10.1175/JCLI3637.1, 2006.

Roberts, M. J., Vidale, P. L., Senior, C., Hewitt, H. T., Bates, C., Berthou, S., Chang, P., Christensen, H. M., Danilov, S., Demory, M.-E., Griffies, S. M., Haarsma, R., Jung, T., Martin, G., Minobe, S., Ringler, T., Satoh, M., Schiemann, R., Scoccimarro, E., Stephens, G. and Wehner, M. F.: The Benefits of Global High Resolution for Climate Simulation: Process Understanding and the Enabling of Stakeholder Decisions at the Regional Scale, Bull. Am. Meteorol. Soc., 99(11), 2341–2359, doi:10.1175/BAMS-D-15-00320.1, 2018.

Roberts, M. J., Baker, A., Blockley, E. W., Calvert, D., Coward, A., Hewitt, H. T., Jackson, L. C., Kuhlbrodt, T., Mathiot, P., Roberts, C. D., Schiemann, R., Seddon, J., Vannière, B. and Vidale, P. L.: Description of the resolution hierarchy of the global coupled HadGEM3-GC3.1 model as used in CMIP6 HighResMIP experiments, Geosci. Model Dev., 12(12), 4999–5028, doi:10.5194/gmd-12-4999-2019, 2019.

Sakamoto, T. T., Komuro, Y., Nishimura, T., Ishii, M., Tatebe, H., Shiogama, H., Hasegawa, A., Toyoda, T., Mori, M. and Suzuki, T.: MIROC4h—a new high-resolution atmosphere-ocean coupled general circulation model, J. Meteorol. Soc. Japan. Ser. II, 90(3), 325–359, 2012.

De Sales, F. and Xue, Y.: Assessing the dynamic-downscaling ability over South America using the intensity-scale verification technique, Int. J. Climatol., 31(8), 1205–1221, doi:10.1002/joc.2139, 2011.

Schneider, U., Becker, A., Finger, P., Meyer-Christoffer, A., Ziese, M. and Rudolf, B.: GPCC's new land surface precipitation climatology based on quality-controlled in situ data and its role in quantifying the global water cycle, Theor. Appl. Climatol., 115(1–2), 15–40, doi:10.1007/s00704-013-0860-x, 2014.

Seth, A., Rojas, M., Liebmann, B. and Qian, J.-H.: Daily rainfall analysis for South America from a regional climate model and station observations, Geophys. Res. Lett., 31(7), doi:10.1029/2003GL019220, 2004.

Shaffrey, L. C., Stevens, I., Norton, W. A., Roberts, M. J., Vidale, P. L., Harle, J. D., Jrrar, A., Stevens, D. P., Woodage, M. J., Demory, M. E., Donners, J., Clark, D. B., Clayton, A., Cole, J. W., Wilson, S. S., Connolley, W. M., Davies, T. M., Iwi, A. M., Johns, T. C., King, J. C., New, A. L., Slingo, J. M., Slingo, A., Steenman-Clark, L. and Martin, G. M.: U.K. HiGEM: The New U.K. High-Resolution Global Environment Model—Model Description and Basic Evaluation, J. Clim., 22(8), 1861–1896, doi:10.1175/2008JCLI2508.1, 2009.

Sierra, J. P., Arias, P. A. and Vieira, S. C.: Precipitation over northern South America and its seasonal variability as simulated by the CMIP5 models, Adv. Meteorol., 2015, 2015.

766 Small, R. J., Bacmeister, J., Bailey, D., Baker, A., Bishop, S., Bryan, F., Caron, J., Dennis, J., Gent, P.,
767 Hsu, H., Jochum, M., Lawrence, D., Muñoz, E., DiNezio, P., Scheitlin, T., Tomas, R., Tribbia, J., Tseng,
768 Y. and Vertenstein, M.: A new synoptic scale resolving global climate simulation using the Community
769 Earth System Model, J. Adv. Model. Earth Syst., 6(4), 1065–1094, doi:doi:10.1002/2014MS000363,
770 2014.

771 Solman, S. A. and Blázquez, J.: Multiscale precipitation variability over South America: Analysis of the
772 added value of CORDEX RCM simulations, Clim. Dyn., 53(3), 1547–1565, doi:10.1007/s00382-019-
773 04689-1, 2019.

774 Sörensson, A. A. and Menéndez, C. G.: Summer soil—precipitation coupling in South America, Tellus A
775 Dyn. Meteorol. Oceanogr., 63(1), 56–68, doi:10.1111/j.1600-0870.2010.00468.x, 2011.

776 Sun, Y., Solomon, S., Dai, A. and Portmann, R. W.: How Often Does It Rain?, J. Clim., 19(6), 916–934,
777 doi:10.1175/JCLI3672.1, 2006.

778 Trenberth, K. E.: Changes in precipitation with climate change, Clim. Res., 47(1–2), 123–138, 2011.

779 Vannière, B., Demory, M.-E., Vidale, P. L., Schiemann, R., Roberts, M. J., Roberts, C. D., Matsueda, M.,
780 Terray, L., Koenigk, T. and Senan, R.: Multi-model evaluation of the sensitivity of the global energy
781 budget and hydrological cycle to resolution, Clim. Dyn., 52(11), 6817–6846, doi:10.1007/s00382-018-
782 4547-y, 2019.

783 Vellinga, M., Roberts, M., Vidale, P. L., Mizielinski, M. S., Demory, M.-E., Schiemann, R., Strachan, J.
784 and Bain, C.: Sahel decadal rainfall variability and the role of model horizontal resolution, Geophys. Res.
785 Lett., 43(1), 326–333, doi:10.1002/2015GL066690, 2016.

786 Vera, C., Higgins, W., Amador, J., Ambrizzi, T., Garreaud, R., Gochis, D., Gutzler, D., Lettenmaier, D.,
787 Marengo, J., Mechoso, C. R., Nogues-Paegle, J., Dias, P. L. S. and Zhang, C.: Toward a Unified View of
788 the American Monsoon Systems, J. Clim., 19(20), 4977–5000, doi:10.1175/JCLI3896.1, 2006.

789 Villamayor, J., Ambrizzi, T. and Mohino, E.: Influence of decadal sea surface temperature variability on
790 northern Brazil rainfall in CMIP5 simulations, Clim. Dyn., 51(1), 563–579, doi:10.1007/s00382-017-
791 3941-1, 2018.

792 Waliser, D. E., Graham, N. E. and Gautier, C.: Comparison of the Highly Reflective Cloud and Outgoing
793 Longwave Radiation Datasets for Use in Estimating Tropical Deep Convection, J. Clim., 6(2), 331–353,
794 doi:10.1175/1520-0442(1993)006<0331:COTHRC>2.0.CO;2, 1993.

795 Walters, D., Baran, A. J., Boutle, I., Brooks, M., Earnshaw, P., Edwards, J., Furtado, K., Hill, P., Lock,
796 A., Manners, J., Morcrette, C., Mulcahy, J., Sanchez, C., Smith, C., Stratton, R., Tennant, W., Tomassini,
797 L., Van Weverberg, K., Vosper, S., Willett, M., Browse, J., Bushell, A., Carslaw, K., Dalvi, M., Essery,
798 R., Gedney, N., Hardiman, S., Johnson, B., Johnson, C., Jones, A., Jones, C., Mann, G., Milton, S.,
799 Rumbold, H., Sellar, A., Ujiie, M., Whitall, M., Williams, K. and Zerroukat, M.: The Met Office Unified
800 Model Global Atmosphere 7.0/7.1 and JULES Global Land 7.0 configurations, Geosci. Model Dev.,
801 12(5), 1909–1963, doi:10.5194/gmd-12-1909-2019, 2019.

802 Wei, J. and Dirmeyer, P. A.: Dissecting soil moisture-precipitation coupling, Geophys. Res. Lett., 39(19),
803 doi:10.1029/2012GL053038, 2012.

804 Wheeler, M. C. and Hendon, H. H.: An All-Season Real-Time Multivariate MJO Index: Development of

an Index for Monitoring and Prediction, Mon. Weather Rev., 132(8), 1917–1932, doi:10.1175/1520-0493(2004)132<1917:AARMMI>2.0.CO;2, 2004.

Williams, K. D., Copsey, D., Blockley, E. W., Bodas-Salcedo, A., Calvert, D., Comer, R., Davis, P., Graham, T., Hewitt, H. T., Hill, R., Hyder, P., Ineson, S., Johns, T. C., Keen, A. B., Lee, R. W., Megann, A., Milton, S. F., Rae, J. G. L., Roberts, M. J., Scaife, A. A., Schiemann, R., Storkey, D., Thorpe, L., Watterson, I. G., Walters, D. N., West, A., Wood, R. A., Woollings, T. and Xavier, P. K.: The Met Office Global Coupled Model 3.0 and 3.1 (GC3.0 and GC3.1) Configurations, J. Adv. Model. Earth Syst., 10(2), 357–380, doi:doi:10.1002/2017MS001115, 2018.

Willmott, C. J., Matsuura, K. and Legates, D. R.: Terrestrial air temperature and precipitation: monthly and annual time series (1950–1999), Cent. Clim. Res. version, 1, 2001.

Yin, L., Fu, R., Shevliakova, E. and Dickinson, R. E.: How well can CMIP5 simulate precipitation and its controlling processes over tropical South America?, Clim. Dyn., 41(11), 3127–3143, doi:10.1007/s00382-012-1582-y, 2013.

Zeng, N., Yoon, J.-H., Marengo, J. A., Subramaniam, A., Nobre, C. A., Mariotti, A. and Neelin, J. D.: Causes and impacts of the 2005 Amazon drought, Environ. Res. Lett., 3(1), 14002, doi:10.1088/1748-9326/3/1/014002, 2008.

Figures

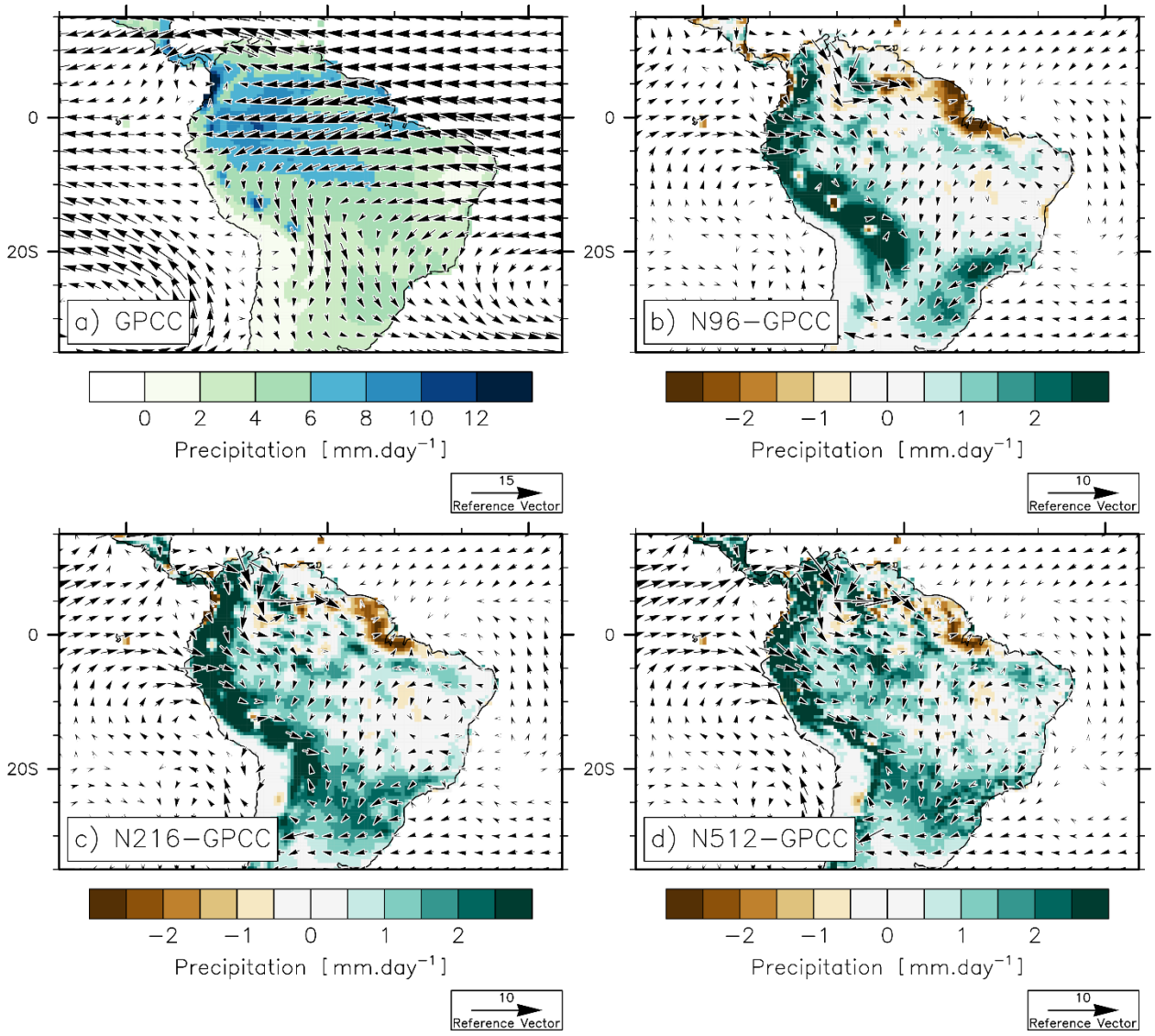

Figure 1: (a) Observed mean annual precipitation (GPCC; mm.day^{-1}; colors) and 850 hPa wind (NCEP; m.s^{-1}; vectors), averaged over the period 1950-2014. Bias in precipitation and 850 hPa wind in (b) N96 (i.e. N96-GPCC), (c) N216 (i.e. N216-GPCC) and (d) N512 (i.e. N512-GPCC). On the panels (a), (b) and (c) biases in precipitation are shown when statistically significant in all of the three members, according to a Student's t-test and a 95% confidence level.

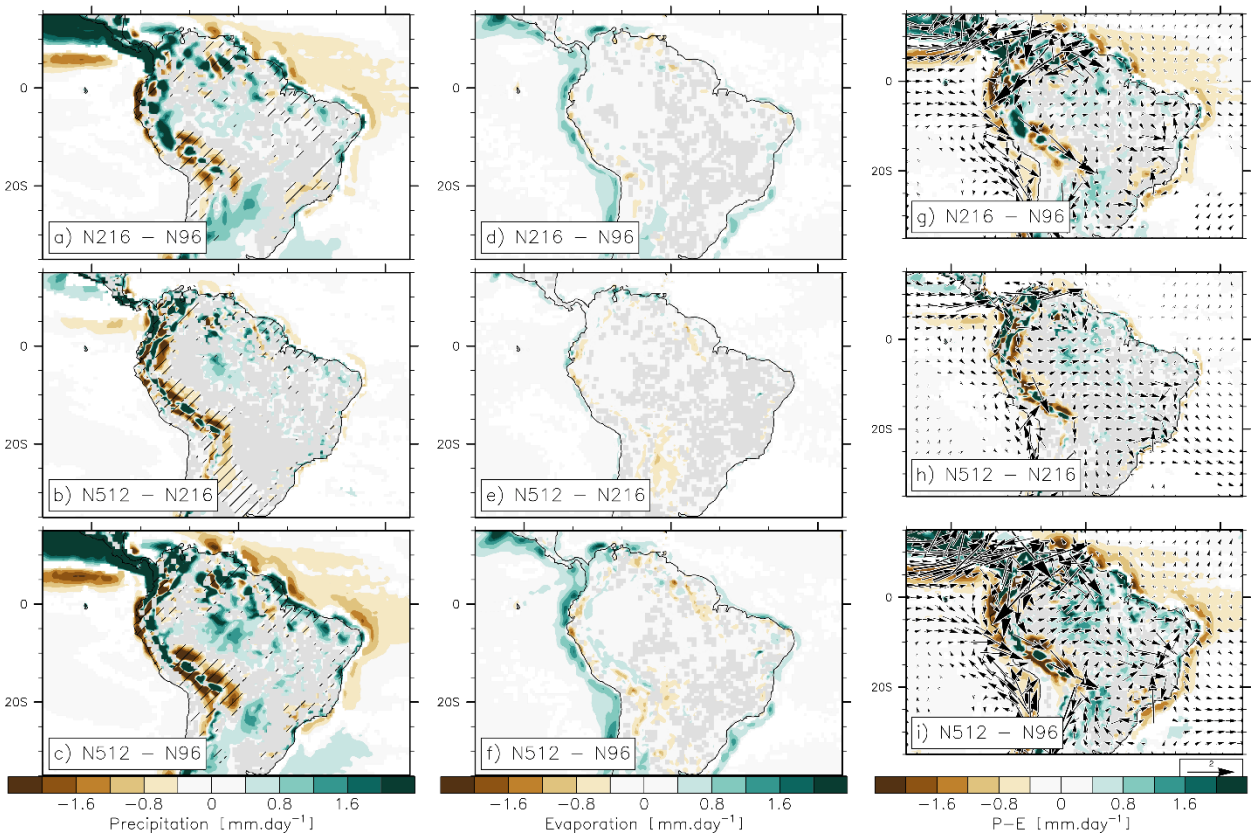

Figure 2: Ensemble-mean (a) N216-N96, (b) N512-N216 and (c) N512-N96 differences in mean annual precipitation (mm.day^{-1}). (d), (e) and (f): same as (a), (b) and (c) but for evaporation (mm.day^{-1}). (g), (h) and (i): same as (a), (b) and (c) but for the moisture flux convergence (P-E; mm.day^{-1}; colors) and the 850 hPa wind (m.s^{-1}; vectors). For precipitation (i.e. left row) stippling indicates that the mean bias is reduced at the higher than at the lower horizontal resolution. Differences are shown when significantly different to zero according to a Student's t-test and a 95% confidence level.

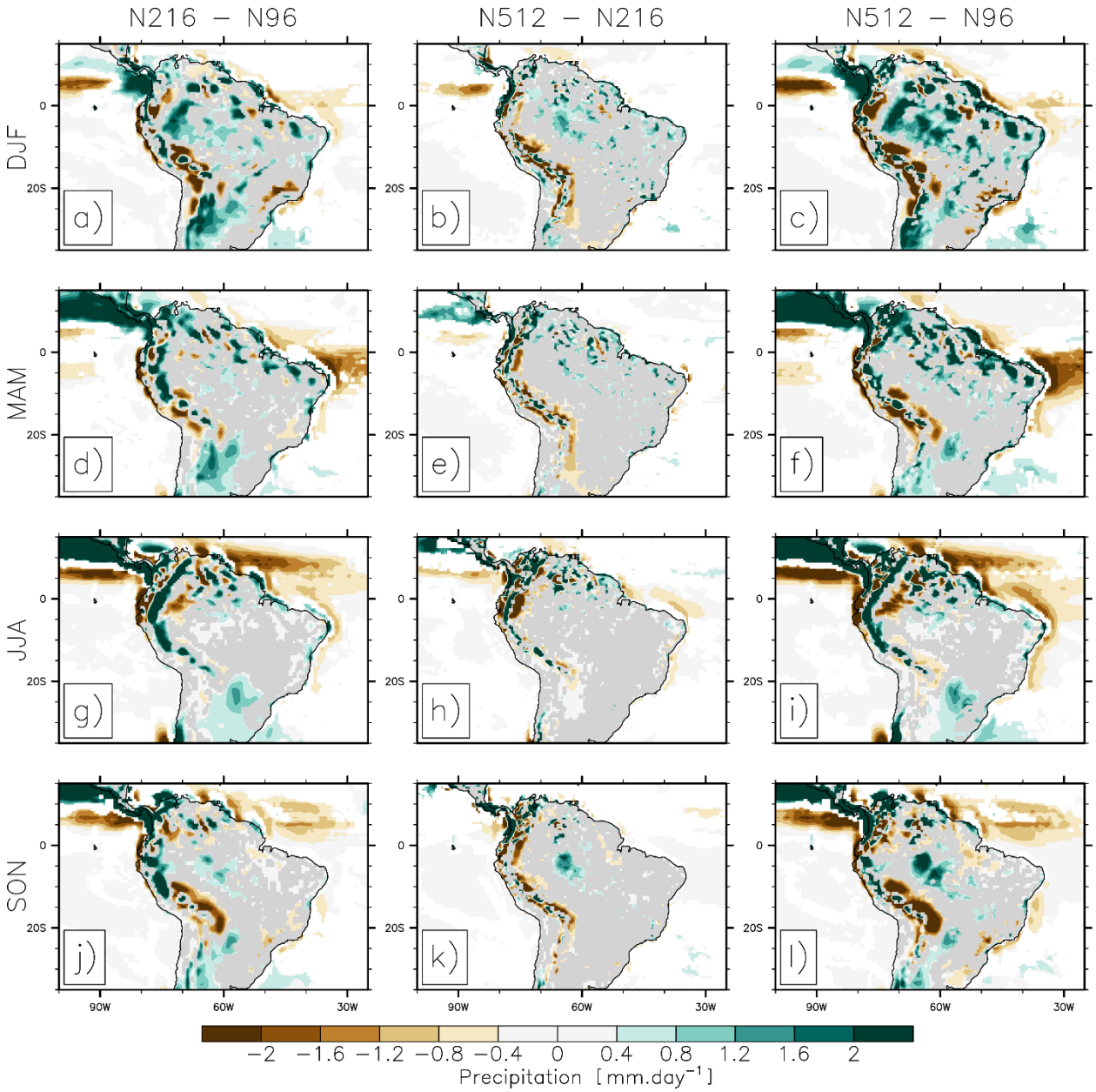

Figure 3: Ensemble-mean N216-N96 difference in (a) DJF, (d), MAM, (g) JJA and (j) SON precipitation ($mm.day^{-1}$). (b), (e), (h) and (k), as in (a), (d), (g) and (j) but for N512-N216. (c), (f), (i) and (l), as in (a), (d), (g) and (j) but for N512-N96. Differences are shown when statistically different to zero, according to a Student's t-test and a 95% confidence level.

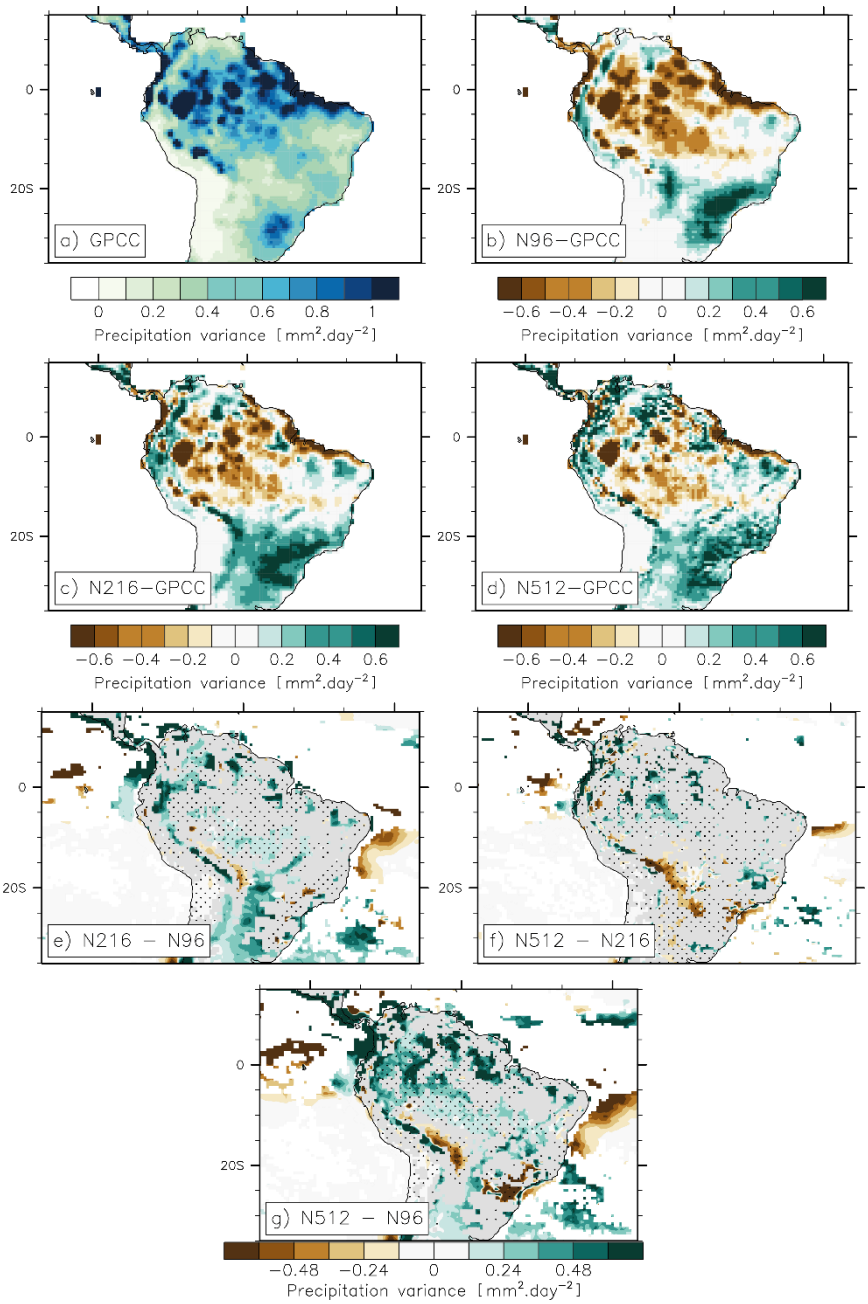

867

868 Figure 4: (a) Observed annual-mean precipitation variance (GPCC; $mm^2.day^{-2}$), as computed over the
869 period 1982-2014. A linear trend is removed. Bias in annual-mean precipitation variance in (b) N96 (i.e.
870 N96-GPCC), (c) N216 (i.e. N216-GPCC) and (d) N512 (i.e. N512-GPCC). (e) N216-N96, (f) N512-N216
871 and (g) N512-N96 differences in annual-mean precipitation variance. On (b), (c) and (d), biases are shown
872 when all three members produces a bias that is significant according to a f-test and a 95% confidence level.
873 On (e), (f) and (g), stippling indicates that the bias is improved at the higher than at the lower resolution.

874

875

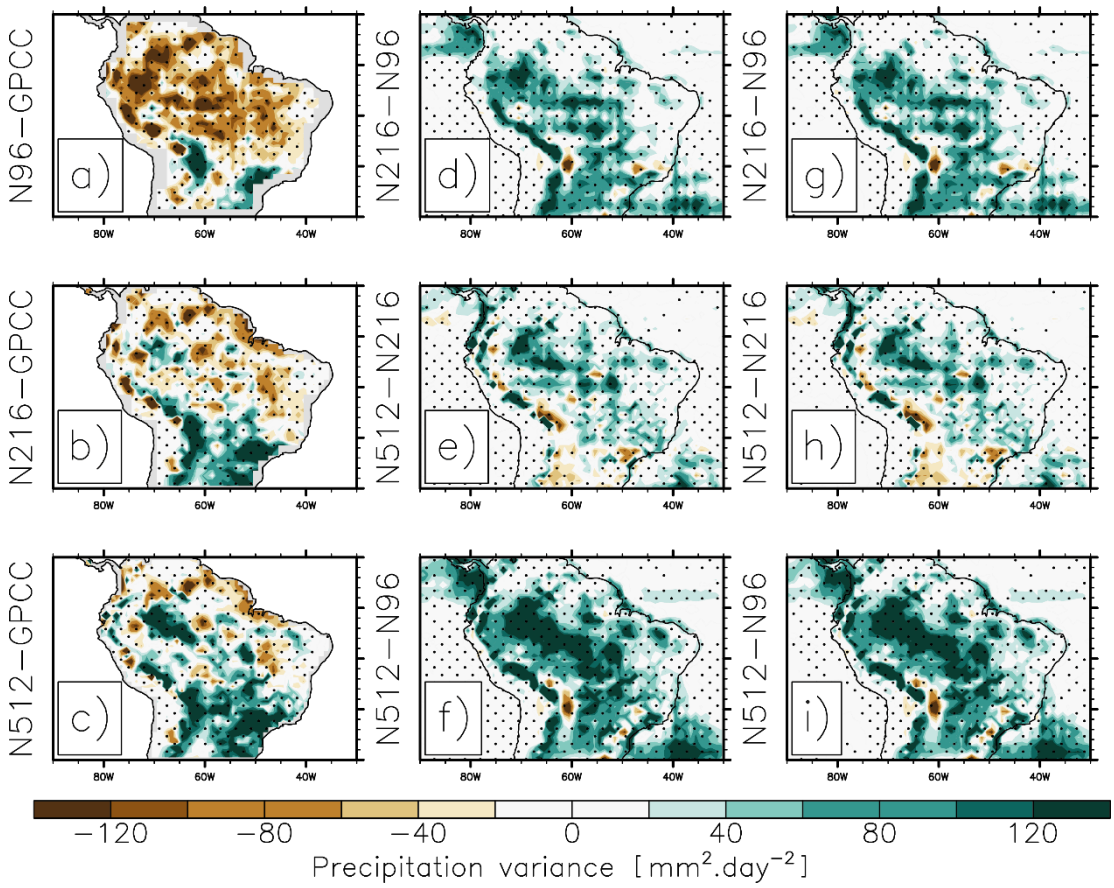

Figure 5: (Left row) Bias in daily precipitation variance ($mm^2.day^{-2}$) for (a) N96 (i.e. N96-GPCC), (b) N216 (i.e. N216-GPCC) and (b) N512 (i.e. N512-GPCC) simulations, over the DJF period. Seasonal cycle and linear trend are removed prior to computing variance. Differences in daily precipitation variance ($mm^2.day^{-2}$) for (d) N216-N96, (e) N512-N216 and (f) N512-N96. (g), (h) and (i), as in (d), (e) and (f) but for P-E (precipitation minus evaporation) variance.

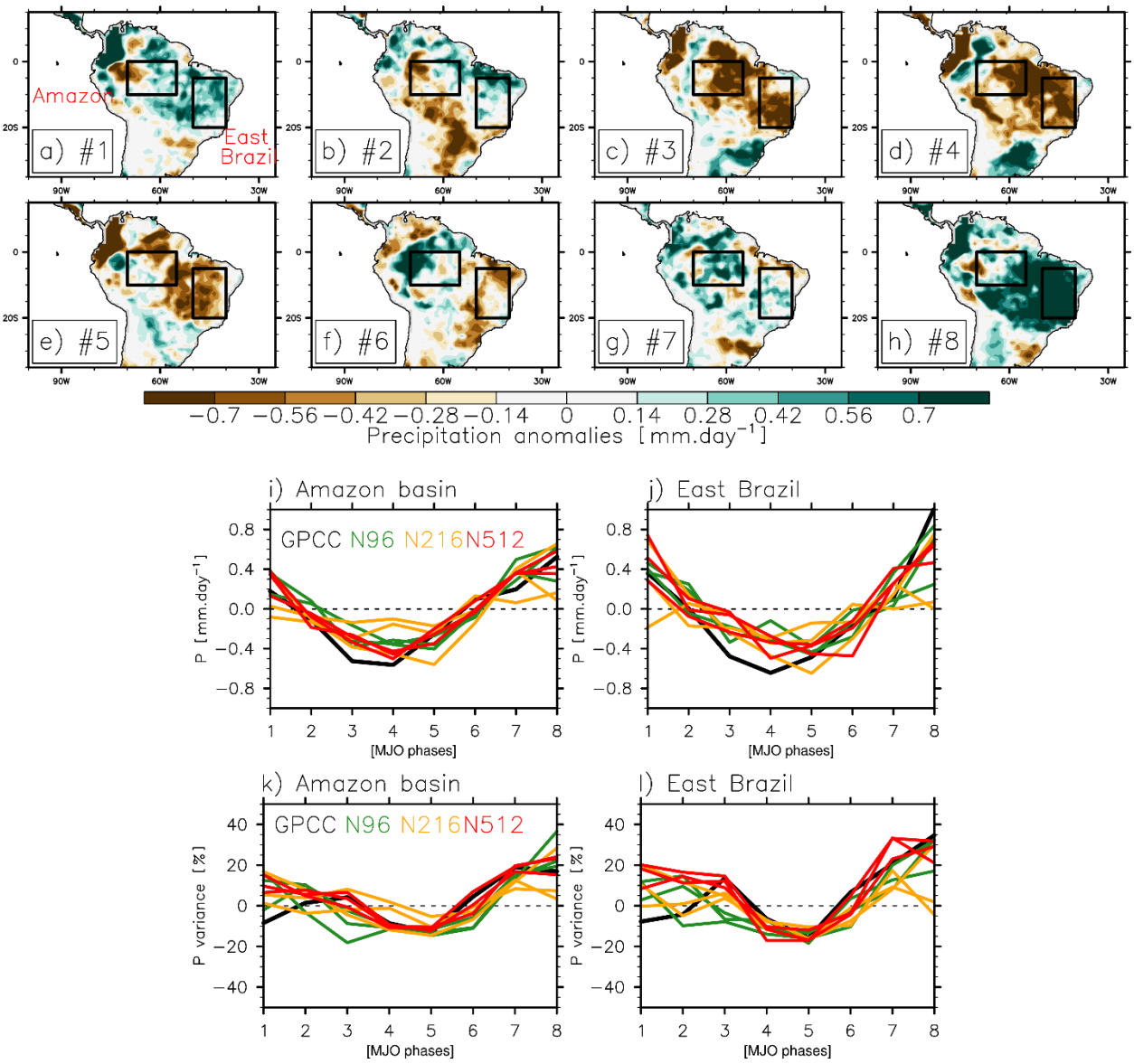

Figure 6: Observed impacts of Madden-Julian Oscillation phase (a) 1, (b) 2, (c) 3, (d) 4, (e) 5, (f) 6, (g) 7 and (h) 8 on precipitation (GPCC and NCEP for the RMM index; mm.day^{-1}). Precipitation anomalies (mm.day^{-1}), associated with each phase of the Madden-Julian Oscillation, relative to the period 1982-2014, and averaged over the (i) Amazon Basin and (j) East Brazil (see the box on (a)), for observation (black), N96 (green), N216 (orange) and N512 (red). (k) and (l), as in (i) and (j) but for precipitation variance, in percent (%) of the precipitation variance over the period 1982-2014.

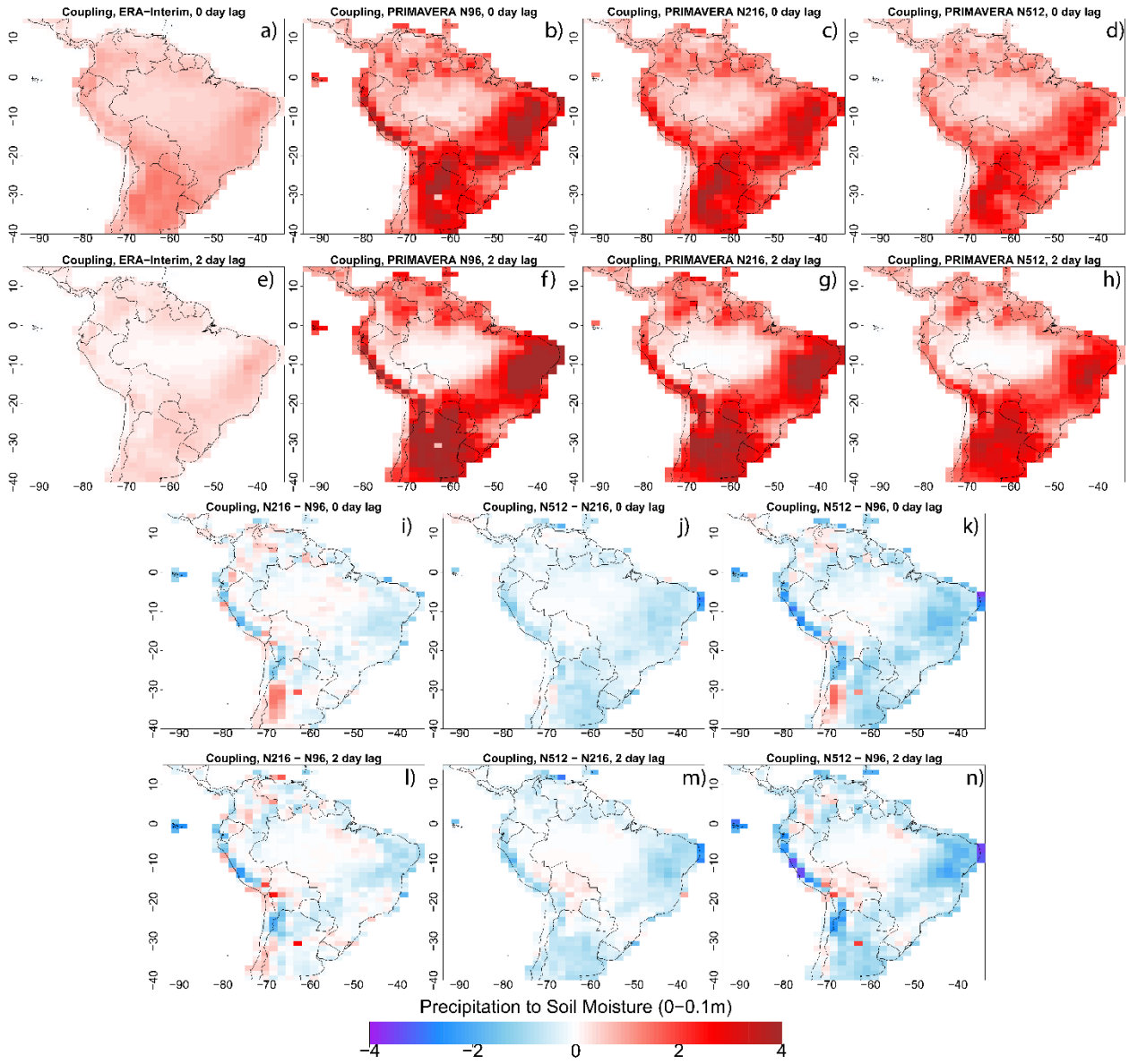

Figure 7: (a) Observed (ERA-Interim) and (b) N96, (c) N216 and (d) N512 Coupling strength ($r_{a,b}\sigma_b$) between daily precipitation and soil moisture (in the top 0.1m of soil) during the southern summer wet season (DJF), over the period 1979-2014. 2-day time lag (i.e. the soil situation 2 days after precipitation) for (e) ERA-Interim, (f) N96, (g) N216 and (h) N512. (i) N216-N96, (j) N512-N216 and (k) N512-N96 coupling strength. (l), (m), (n), as for (i), (j) and (k) but with a 2-day time lag between precipitation and soil moisture.

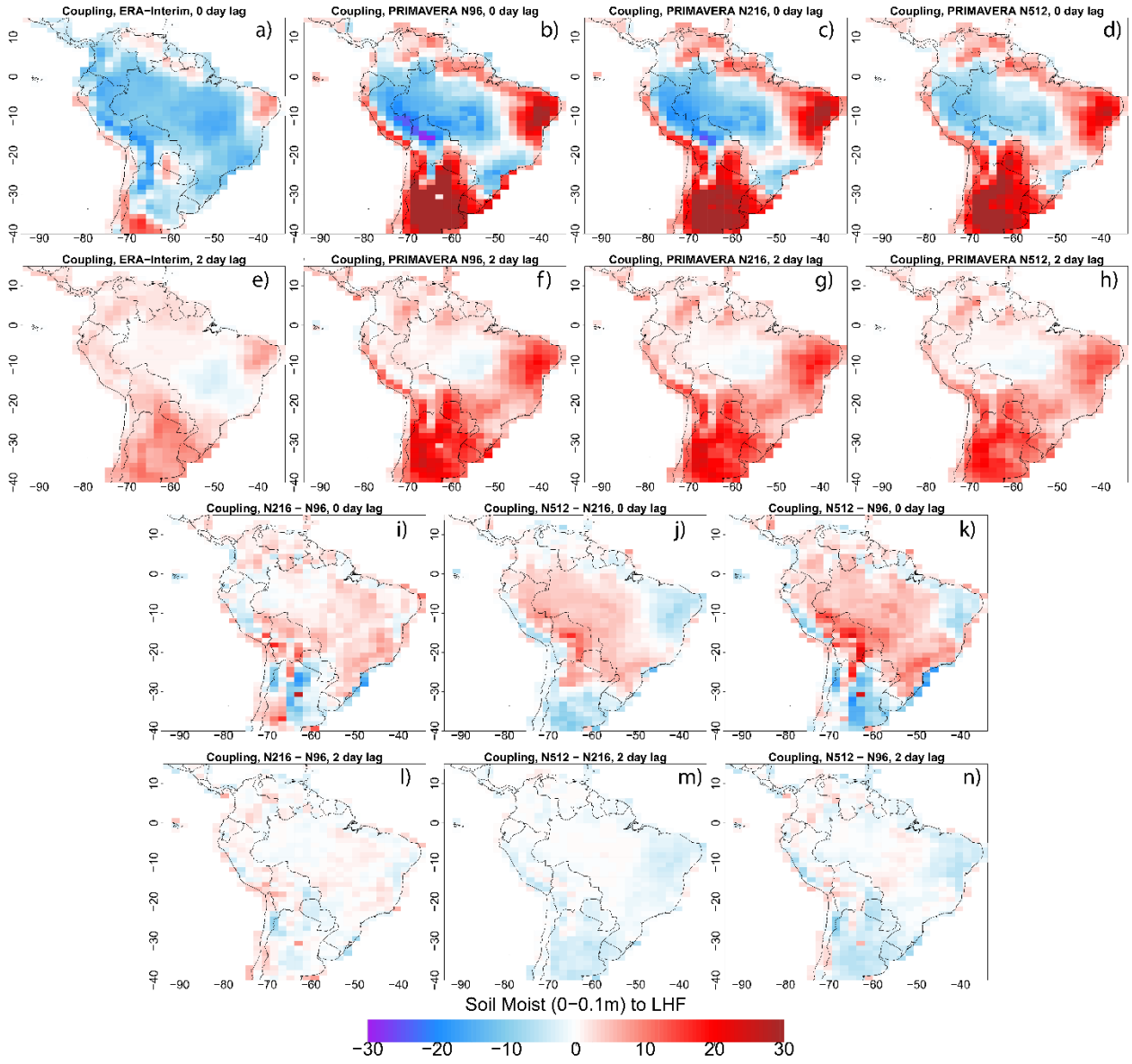

903

904 Figure 8: As in Figure 7 but for the coupling strength between daily soil moisture (in the top 0.1m of
905 soil) and latent heat flux (LHF).

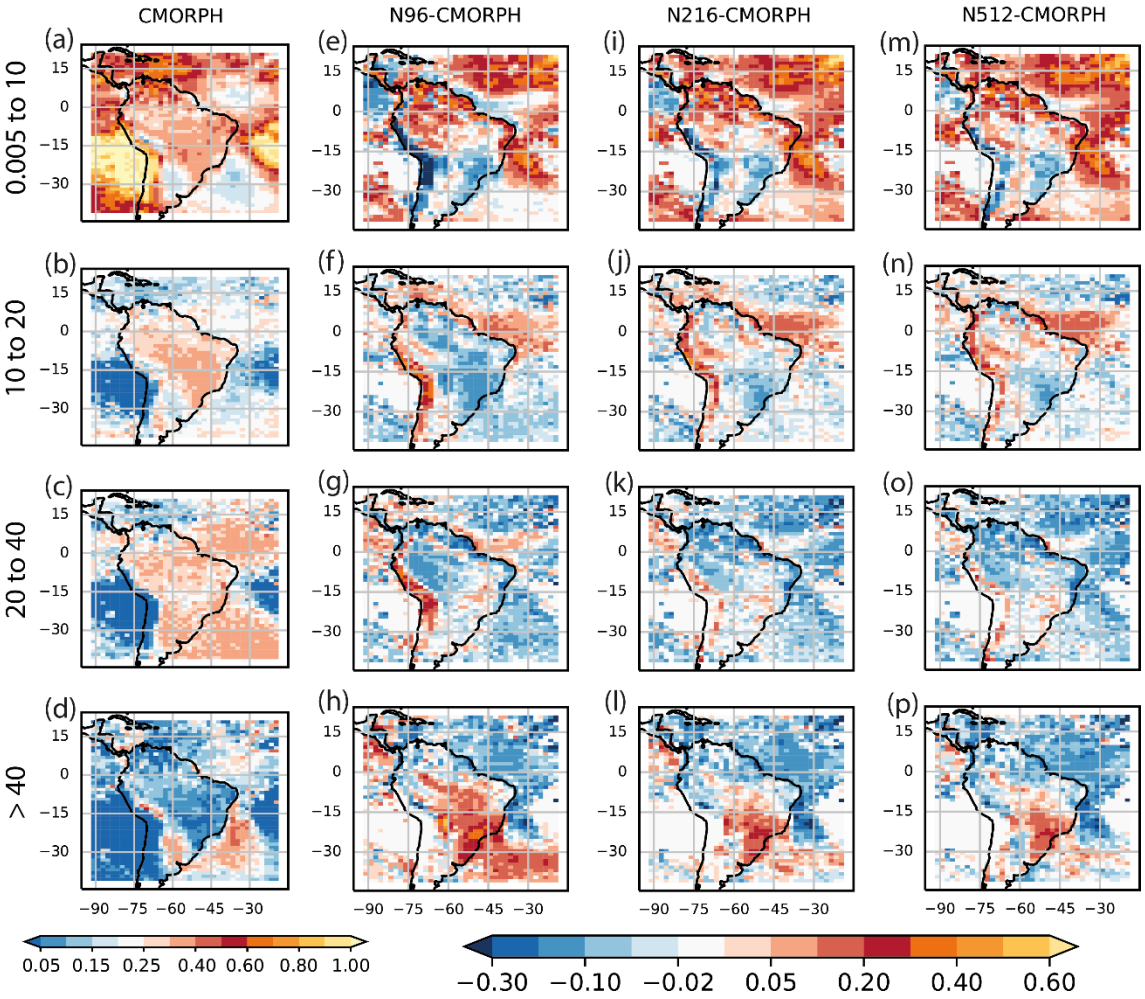

Figure 9: Fractional contribution to the total precipitation from ranges of intensity bins shown in the labels above each panel for CMORPH (a-d) (the sum of each column is unity). Differences in the fractional contributions compared against CMORPH for N96 (e-f), N216 (i-l) and N512 (m-p) all on the N96 common grid. The four ranges of intensity bins are (first row) 0.005 to 10 mm/day, (second row) 10 to 20 mm/day, (third row) 20 to 40 mm/day and (last row) >40 mm.day^{-1}.

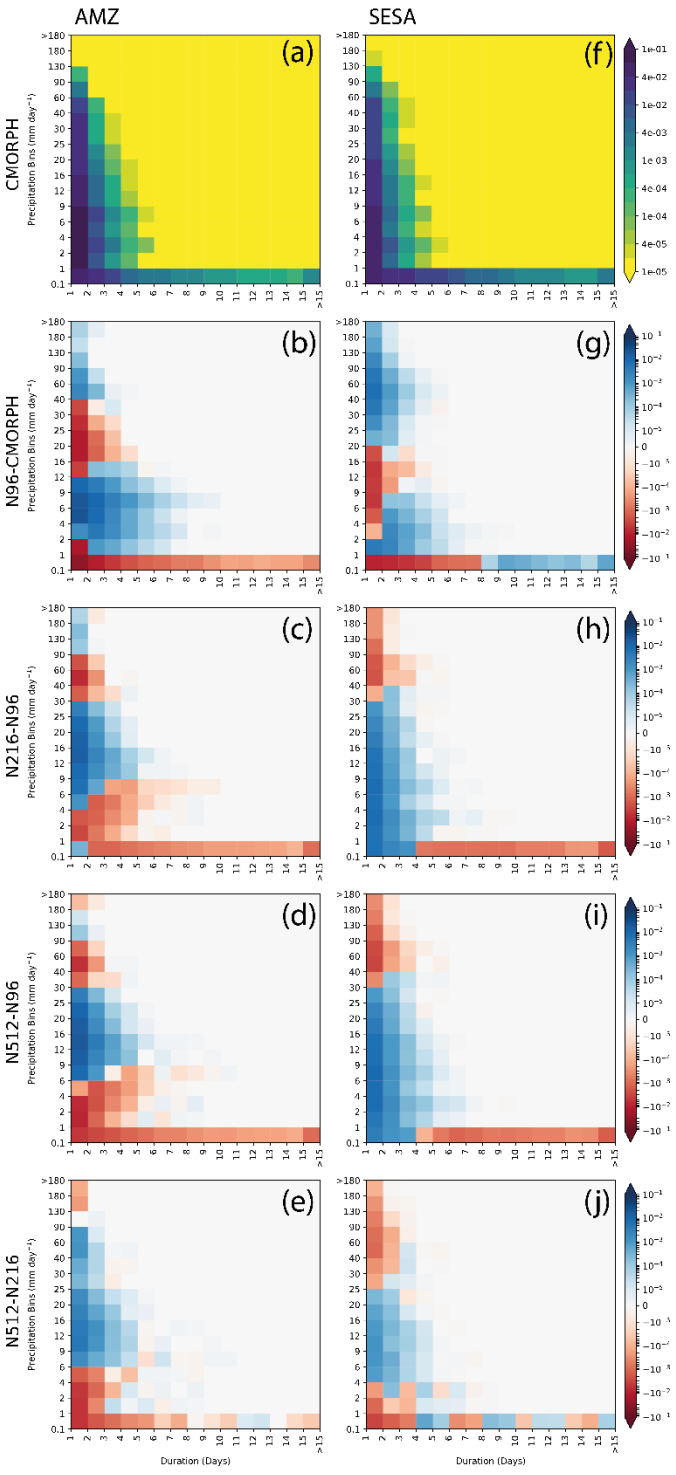

915

916 Figure 10: Two-dimensional histograms of binned precipitation lasting for each duration bin, aggregated
917 over all grid points and normalized by the number of spatial and temporal points in each dataset for (a)
918 CMORPH for the AMZ region at N96 grid. Differences between the two-dimensional histograms for (b)
919 N96 minus CMORPH; (c) N216 minus N96; (d) N512 minus N96 and (e) N512 minus N216 computed on
920 the common N96 grid. (f-j) is same as (a-e) but for the SESA region.

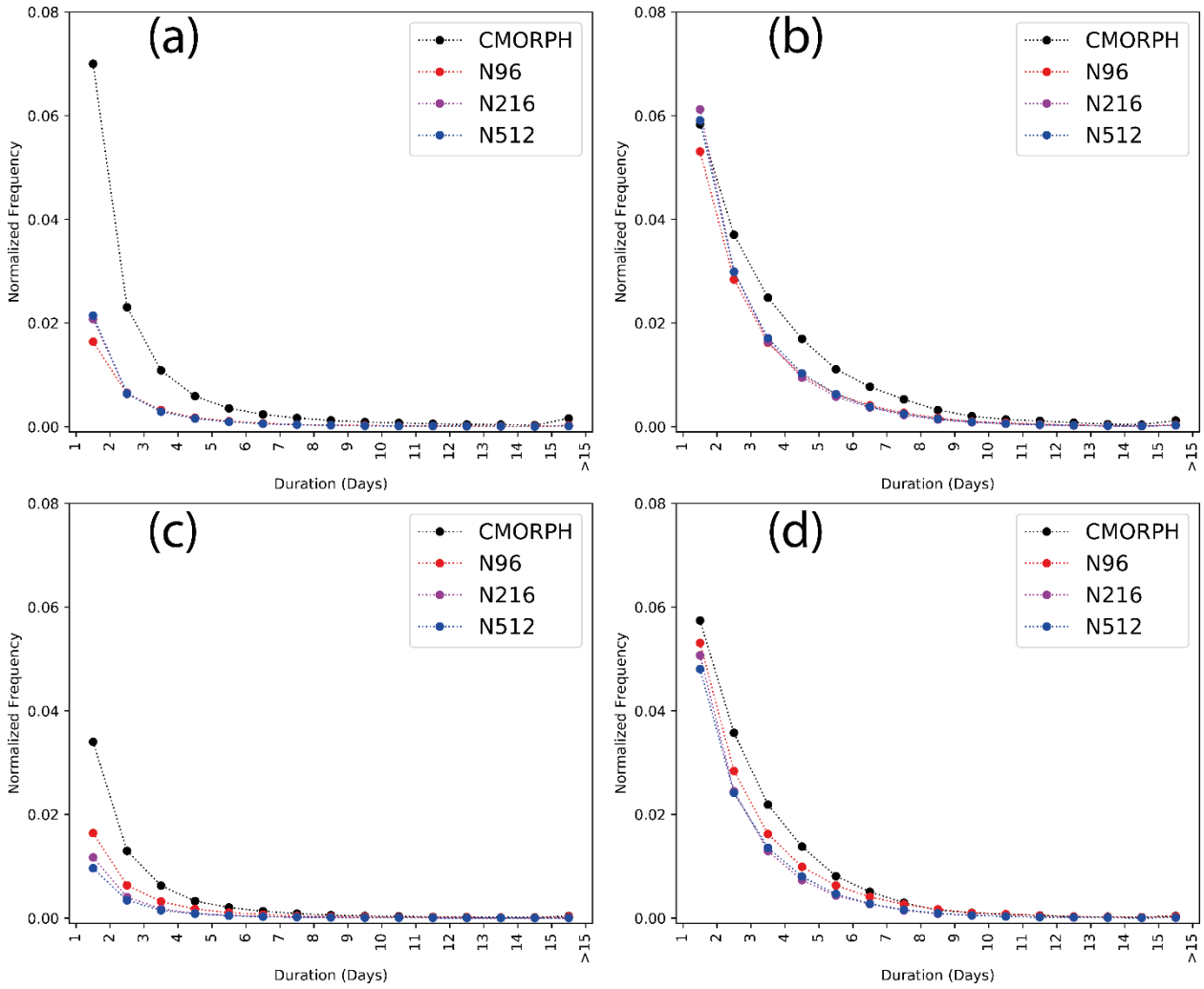

Figure 11: Histograms of dry days (with precipitation less than 0.1 mm day^{-1}) lasting for each duration bin, aggregated over all grid points and normalized by the number of spatial and temporal points in each dataset (a) Amazon and (b) SESA at native resolution for all datasets. (c-d) is same as (a-b) but for datasets on the common N96 grid.

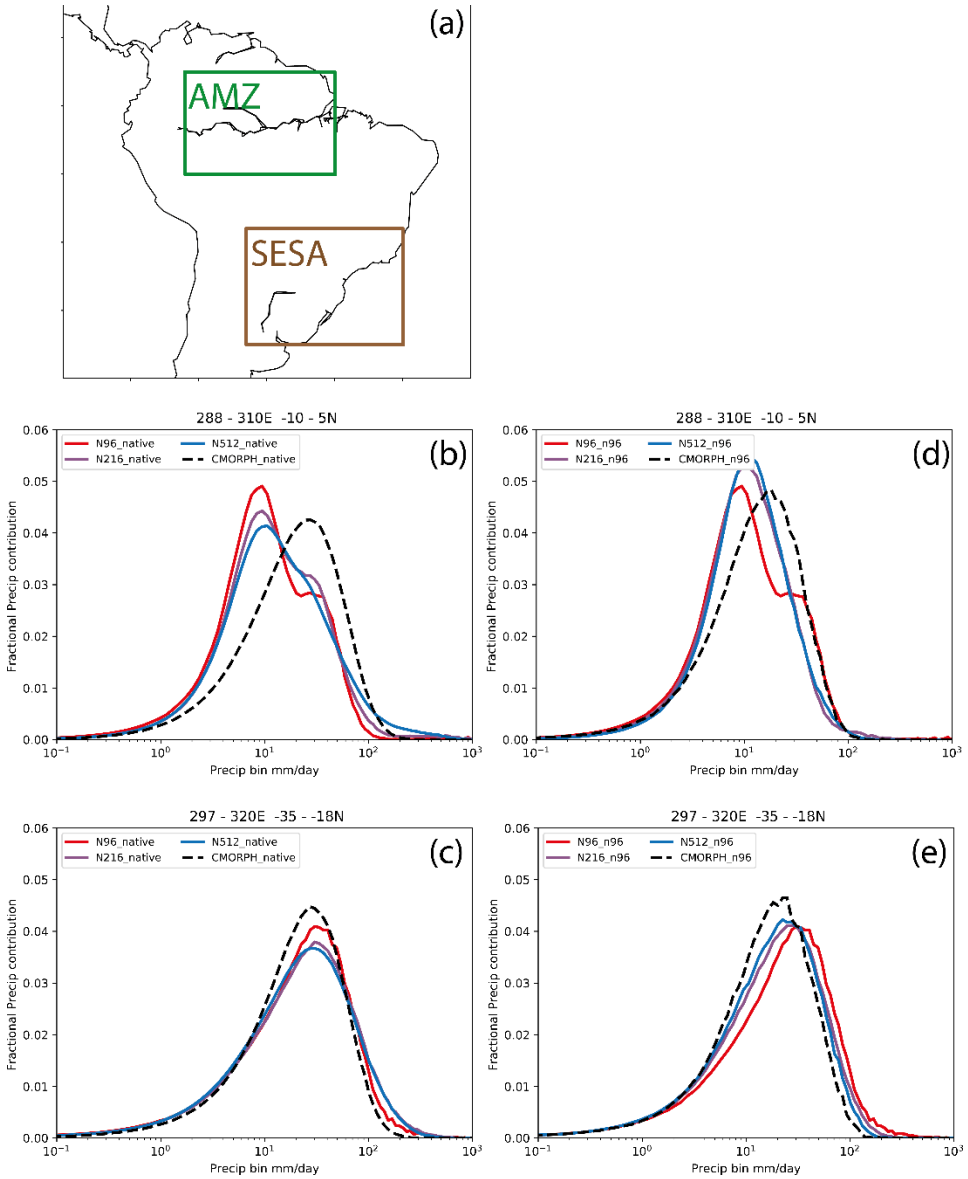

Figure 12: (a) Subregions used in our study (i) the Amazon region (AMZ; green box; 10°S – 5°N; 72°W – 50°W) and (ii) the southeast South America region (SESA; brown box; 35°S – 18°S; 63°W – 40°W). Histograms of the average precipitation contributions to the total precipitation from each precipitation bin for CMORPH and all simulations on their native grids (b) AMZ and (c) SESA. (d-e) is same as (b-c) but at 96 grid.

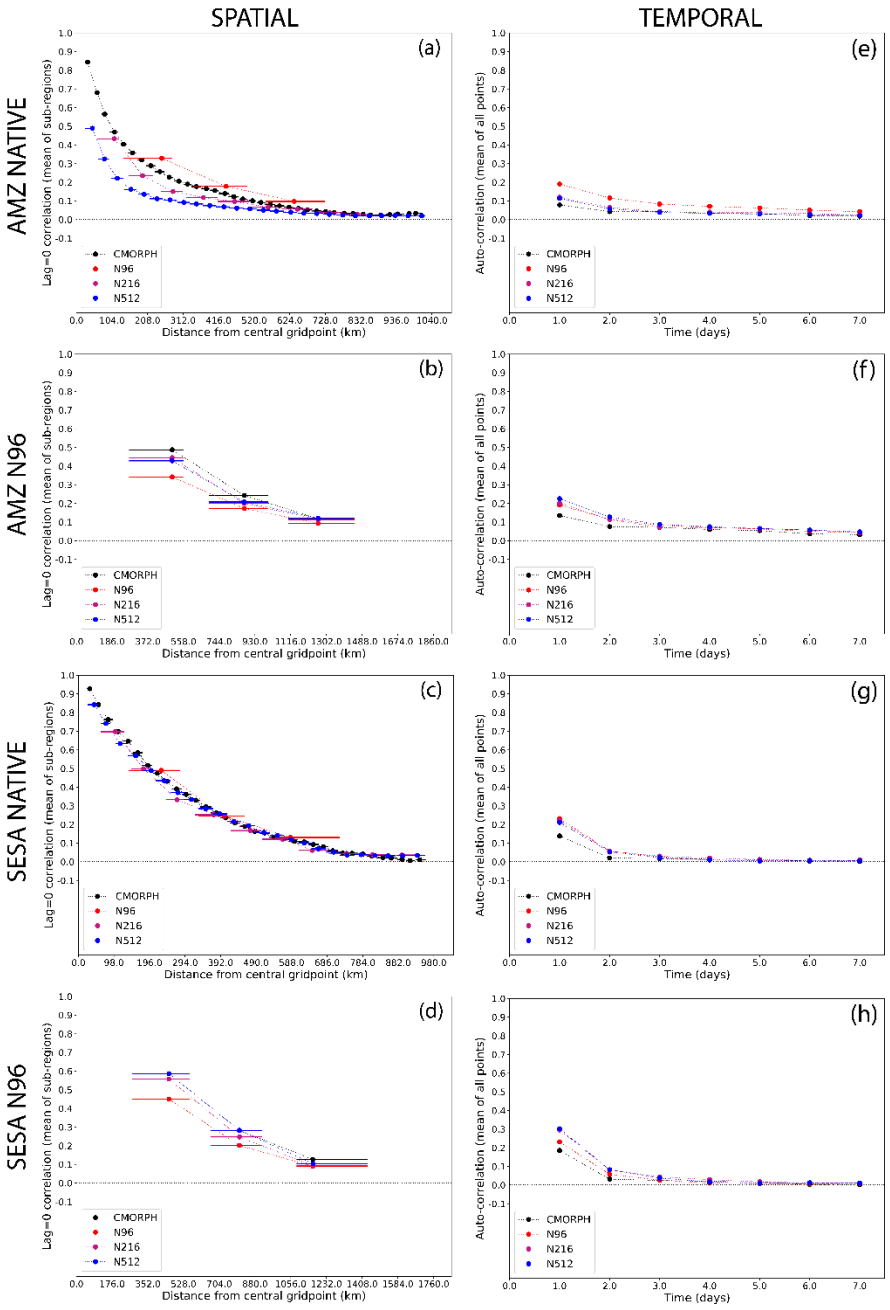

936

937 Figure 13: (a) metric of the spatial scale of daily precipitation (at native resolution), computed by dividing
938 the analysis domain into 1500 km x 1500 km sub-regions and calculating the mean lag-0 correlation
939 between the central grid point and all grid points within each distance bin (which are 1 delta x wide, starting
940 from 0.51x) away from the central grid point, then averaging the correlations over all sub-regions in AMZ;
941 (e) metric of the temporal scale of daily precipitation, computed as the autocorrelation at each point,
942 averaged over all points AMZ. The horizontal lines in (a-d) show the range of distances spanned by each
943 distance bin; the filled circle is placed at the median distance. For clarity, we omit the correlations for zero
944 distance and zero lag, which are 1.0 by definition. (b and f) same as (a and c) respectively for all datasets
945 on the N96 grid; (c-d and g-h) same as (a-b and e-f) respectively but for SESA.